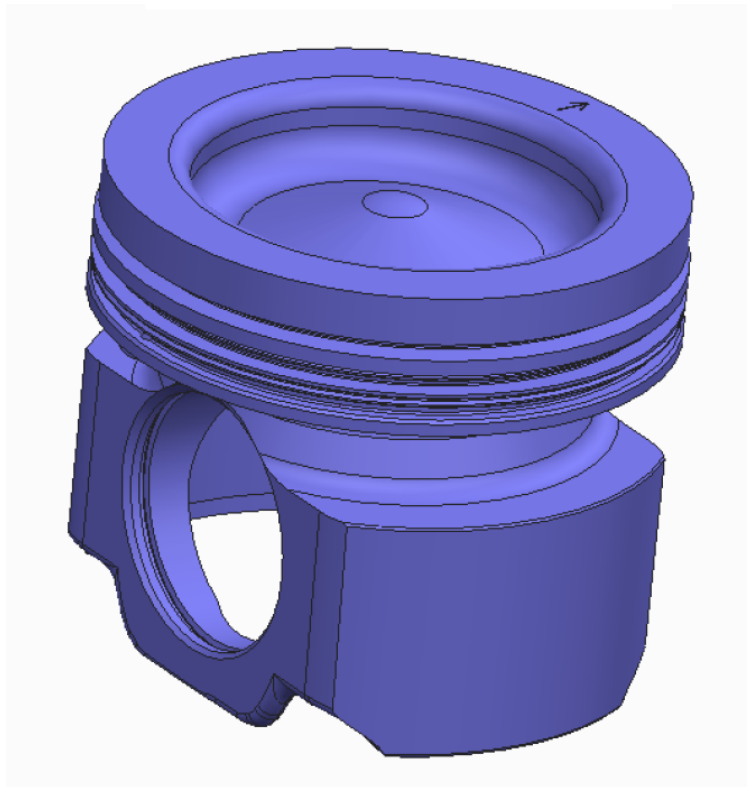




CHALMERS
UNIVERSITY OF TECHNOLOGY



Simulation of piston secondary motion within power cylinder units

Master's thesis in Applied Mechanics

MATHIAS HANSSON
ADAM HERMANSSON

Department of Applied Mechanics
CHALMERS UNIVERSITY OF TECHNOLOGY
Gothenburg, Sweden 2017

MASTER'S THESIS 2017:07

Simulation of piston secondary motion within power cylinder units

Adam Hermansson
Mathias Hansson



CHALMERS
UNIVERSITY OF TECHNOLOGY

Department of Applied Mechanics
CHALMERS UNIVERSITY OF TECHNOLOGY
Gothenburg, Sweden 2017

© Mathias Hansson, Adam Hermansson, 2017. Supervisors: Olsson, B &
Svensson, M & Volvo GTT Powertrain
Examiner: Larsson, F. Applied Mechanics

Master's Thesis 2017:07
Chalmers University of Technology
SE-412 96 Gothenburg
Telephone +46 31 772 1000

Typeset in L^AT_EX
Gothenburg, Sweden 2017

Abstract

This master's thesis concerns the development of a methodology for simulation of piston secondary motion. Firstly, a procedure for performing simulations in a newly developed software is proposed. Secondly, simulations for two particular pistons are carried out to analyze piston secondary motion, piston skirt friction, hydrodynamic pressure in the lubrication oil between the piston and the cylinder liner, the deformation of the piston skirts, and the lubrication oil distribution within a power cylinder unit. The efficiency and robustness of the proposed procedure is illustrated in the simulations of the two pistons. The results show that the software can become a powerful tool when predicting the behavior of pistons inside a power cylinder unit, by comparing the results to real measurements. Furthermore, another goal was to give valuable feedback to the developer to aid the continued work with the software.

Keywords: Piston secondary motion, Power cylinder unit

Acknowledgements

We would like to extend our deepest gratitude to a couple of people, without whom the thesis would have been considerably more difficult to carry out by an order of magnitude. First and foremost we would like to thank Bengt Olsson and Martin Svensson at Volvo GTT Powertrain for presenting us with the opportunity to carry out our master's thesis at Volvo GTT, with a special thanks to Bengt Olsson for his endless help and investment regarding the project. Our deepest gratitude is also extended to Jonathan Hafström, simulation engineer at Volvo GTT, for helping us obtaining finite element analysis data that was crucial to the project. We would also like to thank PhD student Zhen Meng and Dr. Tian at MIT for their continuous help throughout the project regarding discussions about methodology and results. Last, but not least, we would like to thank our examiner Fredrik Larsson at Chalmers University of Technology for helping us during the entire project with everything we asked about and more.

Mathias Hansson and Adam Hermansson, Gothenburg, June 2016

Contents

List of Figures	xi
List of Tables	xiii
1 Introduction	1
1.1 Background	1
1.2 Power Cylinder Unit	1
1.2.1 Piston geometry	4
1.2.2 Lubrication oil and friction	5
1.2.3 Cavitation	6
1.3 Simulation program	7
1.4 Previous work	7
1.5 Purpose	8
1.6 Scope and limitations	8
2 Modeling of the piston secondary motion	9
2.1 The piston primary and secondary motion	9
2.2 Physical models	10
2.2.1 Dynamics and kinematics	10
2.2.2 Hydrodynamic model for the lubrication oil-film	13
2.3 Contact model	15
2.4 Globally convergent Newton's method	16
2.5 Assumptions and simplifications	17
3 Obtaining input data	21
3.1 Piston geometry	21
3.1.1 Radial variation of pistons due to thermal effects	21
3.2 Cylinder liner geometry	22
3.2.1 Radial variation of cylinder liner due to thermal effects	22
3.3 Compliance	23
3.4 Pressure data	25
3.5 Lubricating oil	26
3.5.1 Oil temperature	26
3.5.2 Matching of viscosity models	27
3.6 Coating material	31

Contents

4	Results	33
4.1	Cycle-to-cycle analysis	33
4.2	Piston A	35
4.2.1	Piston secondary motion and general forces	35
4.2.2	Lubrication oil distribution	37
4.2.3	Deformation and pressure distribution	40
4.3	Piston B	46
4.3.1	Piston secondary motion and general forces	46
4.3.2	Lubrication oil distribution	47
4.3.3	Deformation and pressure distribution	47
4.4	Influence of combustion pressure, engine speed, oil splash, and tooling marks	53
4.4.1	Combustion pressure and engine speed parameterization	53
4.4.2	Oil supply parameterization	55
4.4.3	Tooling marks parameterization	56
4.5	Validation of the results	60
5	Conclusions and future work	63
	Bibliography	65
A	Mathematical variables	I

List of Figures

1.1	A power cylinder unit in an exaggerated piston secondary motion deviation.	2
1.2	Explanation of the combustion cycle for a four-stroke engine.	3
1.3	The chamfer data for Piston A and Piston B.	5
1.4	A cylinder liner where cavitation has occurred on the outer wall.	7
2.1	The piston primary and secondary motion.	10
2.2	Free body diagram of the piston with tilting angle ϕ	11
2.3	The model of tooling marks on the piston skirts, taken from [1].	15
3.1	Geometry with exaggerated radial variations of Piston B and Piston A with both cold and hot variation taken into account.	22
3.2	Compliance of the piston.	23
3.3	A figure of the cylinder liner showing the constrained surface, the applied load, and extended liner part.	24
3.4	Compliance of the piston.	24
3.5	Boundary conditions on the piston when obtaining the compliance due to the combustion pressure.	25
3.6	Given combustion pressures from Volvo.	26
3.7	The temperature of the cylinder liner.	27
3.8	The temperature of the lubrication oil at the piston skirt over one combustion cycle.	27
3.9	The dynamic viscosity according to Volvo's viscosity model and the software's viscosity model for varying temperature.	29
3.10	The difference between Volvo's viscosity model and the software's viscosity model before and after matching of the correlation constants.	30
3.11	The percentage change between the two viscosity models before and after the matching of the correlation constants.	30
4.1	Cycle-to-cycle variance for lateral motion, tilting angle, and force acting on the piston B from the wrist-pin.	34
4.2	Differences and meanvalues between the four combustion cycles for lateral motion y , tilting angle ϕ , and force F_{ywp2ps} acting on the piston B from the wrist-pin.	35
4.3	Lateral and tilting motion for the piston A.	36
4.4	Frictional power and energy loss for the piston A.	36

List of Figures

4.5	Six figures showing asperity contact, side force $F_{y_{wp2ps}}$ and frictional force for the fictional piston.	37
4.6	Simulation of lubrication oil distribution for the piston A at 1200 rpm at different crank angles in the interval $[0, 300]^\circ$	42
4.7	Simulation of lubrication oil distribution for the piston A at 1200 rpm at different crank angles in the interval $[370, 720]^\circ$	43
4.8	Asperity contact pressure (first column), Deformation (second column) and hydrodynamic pressure (third column) on the thrust side on the piston A for the crank angles 360° , 390° , 420° and 450°	44
4.9	Asperity contact pressure (first column), Deformation (second column) and hydrodynamic pressure (third column) on the thrust side on the piston A for the crank angles 480° , 510° , 540° and 570°	45
4.10	Lateral and tilting motion of the piston B.	46
4.11	Frictional power and energy loss for the piston B.	47
4.12	Six figures showing asperity contact, side force $F_{y_{wp2ps}}$ and frictional force for the fictional piston.	48
4.13	Simulation of lubrication oil distribution for the piston B at 900 rpm at different crank angles in the interval $[0, 300]^\circ$	49
4.14	Simulation of lubrication oil distribution for the piston B at 900 rpm at different crank angles in the interval $[370, 720]^\circ$	50
4.15	Asperity contact pressure (first column), Deformation (second column) and hydrodynamic pressure (third column) on the thrust side on the piston B for the crank angles 360° , 390° , 420° and 450°	51
4.16	Asperity contact pressure (first column), Deformation (second column) and hydrodynamic pressure (third column) on the thrust side on the piston B for the crank angles 480° , 510° , 540° and 570°	52
4.17	Lateral and tilting motion for the piston B for 900, 1200 and 1800 rpm.	53
4.18	Total side $F_{y_{wp2ps}}$ and friction forces for the piston B for 900, 1200, and 1800 rpm.	54
4.19	Frictional power and accumulated frictional energy loss for the piston B for 900, 1200 and 1800 rpm.	55
4.20	Parameterization on Oil splash for the piston B - Lateral and tilting motion.	56
4.21	Parameterization on Oil splash for the piston B - Total side $F_{y_{wp2ps}}$ and friction forces.	57
4.22	Parameterization on Oil splash for the piston B - Frictional losses.	58
4.23	Parameterization on the wave height for the piston skirt for the piston B - lateral and tilting motion.	58
4.24	Parameterization on the wave height for the piston skirt for the piston B - Total side and friction forces.	59
4.25	Parameterization on the wave height for the piston skirt of the piston B - Frictional Losses	59
4.26	Normal forces from the study <i>The Effects of Piston Skirt</i> [2].	60

List of Tables

1.1	Table of the specific parts in Figure 1.1 which are directly relevant for this master thesis.	4
2.1	Unknown variables in the conclusive Equations (2.1) and (2.6).	16
2.2	Assumptions and simplifications related to the theory.	19
3.1	The given data for the Piston A, Piston B, 10W-30 Oil and the initial oil values for the cylinder liner.	21
3.2	Dynamic viscosity at shear rate 10^6s^{-1} for the 10W-30 oil.	28
A.1	Summary of the stated mathematical terms in order of apperence in the thesis.	I

List of Tables

1

Introduction

This section aims to give the reader sufficient knowledge about the power cylinder unit (what it is, how it works, and how the parts in the system work together) in order to understand the theory regarding the software and the method used when carrying out the simulations.

1.1 Background

The heart of all trucks is the engine. In the case of diesel engines there are cylinders in which pistons are moved up and down due to combustion of fuel, which in turn generates the power needed to move the truck forward. The pistons moving up and down in the cylinders are connected to a crankshaft through connecting rods, and together the piston and cylinder create a *power cylinder unit* (PCU), see Figure 1.1. How these pistons move is of importance since it affects the efficiency of the engine, vibrations in the engine, wear on the pistons, as well as oil distribution in the power cylinder unit. Since experiments and measurements are expensive to carry out and inflexible in determining one single parameter's effects on the system, it is of great interest to get ahold of this data by computational simulations. The purpose of this report is thus to compare two different power cylinder units, with two different types of pistons, with respect to *piston secondary motion*, *piston skirt friction*, *lubrication oil distribution*, and *pressure on the cylinder liner*, with the help of computational simulations.

The analyzes were carried out with a software which is under development at MIT (Massachusetts Institute of Technology). The software is a part of a larger research work regarding the components in a combustion engine, and its strength lies in calculating the influence of the piston secondary motion with regard to friction, pressure distribution and lubrication oil distribution. The work presented in this report was carried out with support from the current developer of the software, PhD student Zhen Meng at MIT, and with constant support from Volvo GTT Powertrain Engineering.

1.2 Power Cylinder Unit

Figure 1.1 shows a setup of a piston moving in a cylinder liner, connected to a crankshaft by a connecting rod, i.e. a power cylinder unit. Note that if you change the type of piston inside the cylinder liner then the system is considered to be a new power cylinder unit. That is, two different types of pistons are considered

1. Introduction

which make two different types of power cylinder units even though the cylinder liner is the same. How detailed the power cylinder units are with regard to included components is shown in Table 1.1.

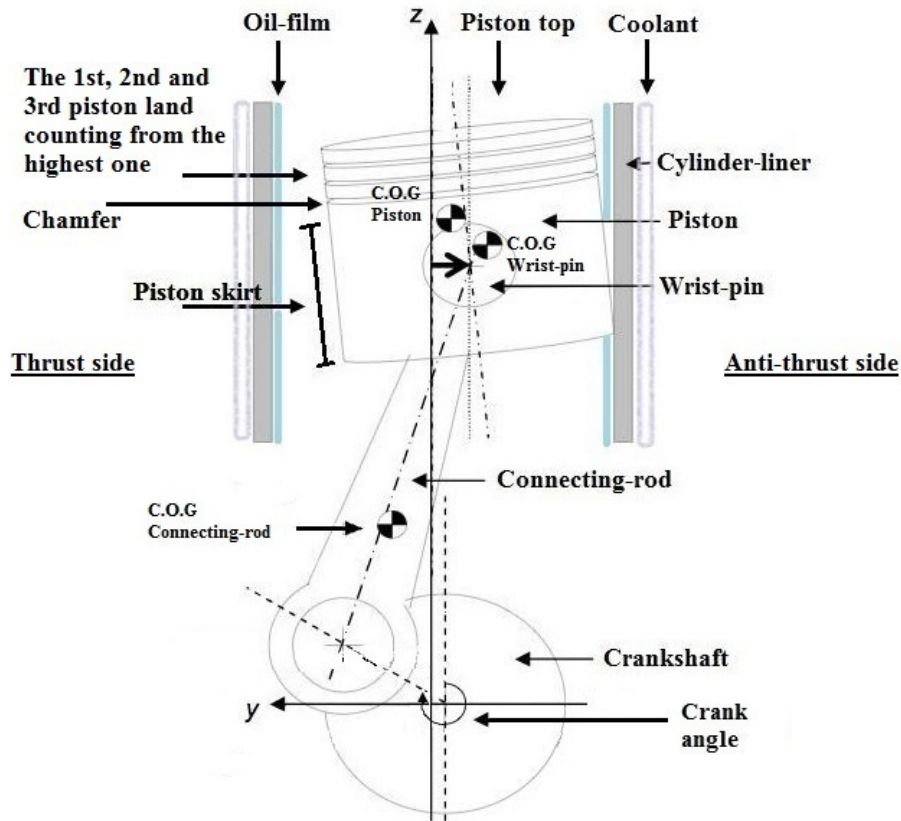


Figure 1.1: A schematic figure of a power cylinder unit in an exaggerated piston secondary motion deviation where COG refers to the center of gravity for the specific parts. The distance between the piston and cylinder liner is also exaggerated. Between the lands there are piston rings located but are not included in this figure.

The motion of the piston is mainly influenced by the combustion pressure and at which *crank angle* (CA, see Figure 1.1) the connecting rod is positioned. For a four-stroke engine, which is the engine type this report concerns, one combustion cycle is defined by the piston making four complete strokes which means that the crankshaft makes two revolutions, or quantitatively 720° . The piston subsequently reaches *top dead center* (TDC) and *bottom dead center* (BDC) two times during each combustion cycle. TDC and BDC simply correspond to the highest and lowest locations of the piston during the combustion cycle, respectively. Thus, the name *four-stroke engine* refers to number of piston strokes for each combustion cycle. The

combustion cycle is represented quantitatively in the extreme points

$$\begin{array}{ccccccc} & \underbrace{\text{TDC}} & & \underbrace{\text{TDC}} & & \underbrace{\text{TDC}} & \\ & \text{0} & , & \text{180} & , & \text{360} & , & \text{540} & , & \text{720} &]^\circ \\ & & & \underbrace{\text{BDC}} & & \underbrace{\text{BDC}} & & & & & \end{array} \quad (1.1)$$

In this master thesis, when *combustion cycle* is mentioned it refers to a combustion cycle in a four-stroke engine.

In order to understand how the power cylinder unit works, the combustion cycle can be split up into four phases, namely, *Intake-phase* (#1), *Compression-phase* (#2), *Combustion-phase* (#3), and *Exhaust-phase* (#4), in chronological order. Figure 1.2 shows a combustion cycle for a four-stroke engine.

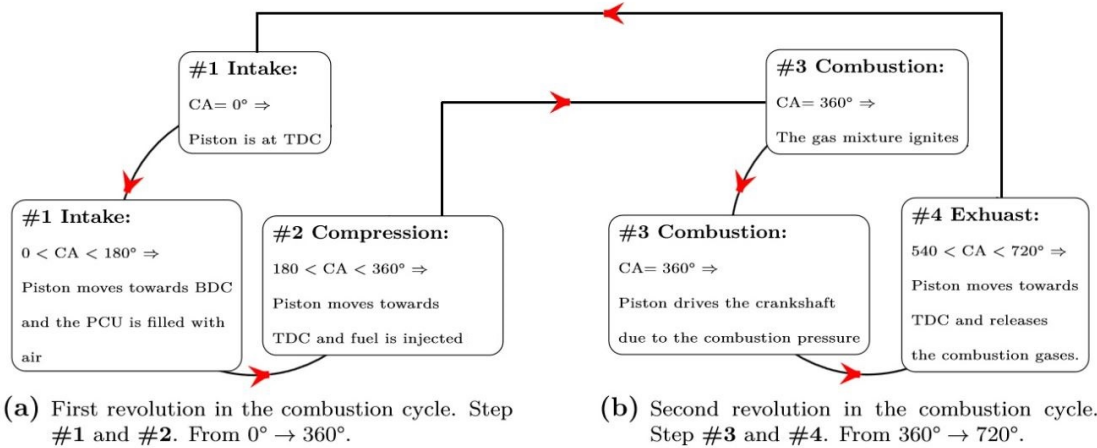


Figure 1.2: Explanation of the combustion cycle for a four-stroke engine.

At the beginning of the combustion cycle, where the CA is 0°, the piston is located at TDC. As the piston moves towards BDC air is filled in the power cylinder unit through the intake valves until the connecting-rod reaches crank angle 180°. Thus, for crank angles in between 0° < CA < 180°, the power cylinder unit is in the Intake-phase.

When the crank angle is in between 180° < CA < 360° the intake valves are closed and the Compression-phase begins. As the piston moves close to TDC fuel is injected into the combustion chamber. When the piston reaches TDC the second time, the fuel is ignited due to the compression (for a diesel engine). The internal energy of the fuel is then transformed into mechanical work by the piston. That is, when the fuel burns, a pressure is created which drives the crankshaft. This process corresponds to the Combustion-phase.

Lastly, when the crank angle is in between 540° < CA < 720° the Exhaust valves open and the Exhaust-phase begins. The piston moves towards TDC and releases the exhaust gases that are left over from the combustion in the power cylinder unit. With the Exhaust-phase completed, a new combustion cycle is started and the process starts over with the Intake-phase. However, during the combustion

1. Introduction

cycle, the motion of the piston does not coincide perfectly with the centerline of the cylinder liner (see Figure 2.1), which creates friction between the piston and the cylinder liner. This can be read about in Section 1.2.2.

Table 1.1: Table of the specific parts in Figure 1.1 which are directly relevant for this master thesis. The ones with blue background denote the parts which explicitly define the power cylinder unit.

Part	Considered in this thesis (×)
cylinder liner	×
Piston	×
wrist pin	×
Piston rings ^a	-
Oil cooling jet ^b	-
Crank angle (CA)	×
Connecting-rod	×
Crankshaft	×
Oil-film	×
Piston top	×
Coolant	-
Piston skirt	×
Top land	-
2nd land	×
3rd land	-
4th land	-
C.O.G Piston	×
C.O.G wrist pin	×
C.O.G Connecting-rod	×

^aNot included in Figure 1.1 but is included in the definition of the power cylinder unit.

^bNot included in Figure 1.1 and this master thesis, but is sometimes included in the definition of the power cylinder unit.

1.2.1 Piston geometry

The project has included two different pistons, Piston A and Piston B, both of which are 131 mm in diameter, made out of steel, and weigh about 3.3 kg.

Observing the geometry of these two pistons, the pistons are constructed in such a way that the piston skirt is not perfectly vertical. In reality they have a convex "barrel-shape" geometry that, although isn't very prominent, can influence the results. Secondly, the surface of the piston skirt has triangular tooling marks

from the machining that run in the circumferential direction. The magnitude of these toolings marks is generally believed to be in the same size as the oil film thickness and are schematically shown in Figure 2.3. If the lateral force on the piston is sufficiently large, this can lead to the tooling marks penetrating the oil film, making the piston skirt come in direct contact with the cylinder liner. Also, since the source of heat is on the top of the piston, then the temperature in the piston will increase with increasing z-direction (see Figure 1.1), which means that the upper part of the piston is affected more by the combustion compared to the bottom part.

Just above the piston skirt an area with a radius smaller than the piston skirt is located. As the piston moves up and down during operation, lubrication oil thus has the possibility of accumulating here, making it work like a reservoir for the oil supply to the pistons. Piston A has a much larger chamfer compared to Piston B, and therefore the ability to store more lubrication oil in the chamfer. Above the area

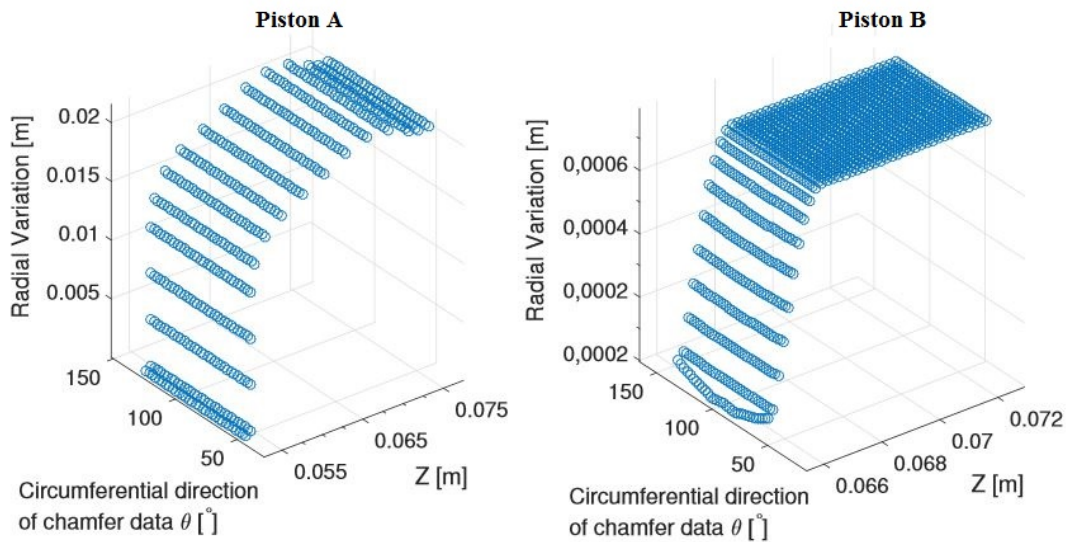


Figure 1.3: The chamfer data for Piston A and Piston B.

with smaller radius than the piston skirt there are lands located which determine the distance between the piston rings. These lands can also come in contact with the cylinder liner, and for that reason also influence the friction in the PCU. By looking at used pistons it has been determined that the 2nd land is the land that comes most in contact with the cylinder liner, and it was therefore the only land that was included in the simulations.

1.2.2 Lubrication oil and friction

The total friction, or piston-cylinder liner-friction, in the PCU can be divided into two different main types of friction: the piston ring friction and piston skirt friction. This master thesis aimed to analyze the piston skirt friction including the 2nd land,

1. Introduction

since the software is limited to the skirt and the lands. That is, the software is currently not developed for taking the piston rings into account, which is treated in other programs made by the developing team, Section 1.1.

In order for the piston to move as smoothly as possible in the cylinder liner, lubrication oil is present in the engine. How the oil is distributed in the PCU is called lubrication oil distribution. During operation, the oil is present on both the cylinder liner and piston. The distribution of the lubrication oil, and how it changed during the combustion cycle, is an area that the project aimed to study.

In rough terms, direct contact between piston and cylinder liner can lead to high friction, and as a result abrasion within the PCU. This damages both the cylinder liner and piston, and thus, can advance the wear in both components. If the wear becomes extensive, there is a risk of a reduction in efficiency, but also for failure of the power cylinder unit, which is expensive and time-consuming. This master thesis does not consider the physical phenomenon of abrasion directly, but the analyzes of friction from simulations can lead to a better knowledge of the locations where the contact pressure becomes high in the power cylinder unit, so that it indicates where it is likely that wear could occur.

1.2.3 Cavitation

Cavitation is a phenomenon that arises due to vapor bubbles in a liquid, which come into existence due to rapid changes of the pressure in the liquid. Over time, when these bubbles implode near the surface they create a cyclic load which can wear the surface down.

It is empirically known that cavitation arises on the outside of the cylinder liner, where the coolant comes in contact with the cylinder liner. For continuous driving conditions the contact between piston and cylinder liner tends to occur at the same place, which leads to cavitation developing at a specific location over and over. Thus, larger manifestations of piston secondary motion increases the probability of cavitation-wear in the cylinder liner outer wall. Figure 1.4 shows a cylinder liner in which cavitation has occurred.

The knowledge of how the piston secondary motion behaves is therefore important in order to understand the friction and pressure between the piston and the cylinder liner, and lubrication oil distribution, which are three of the physical phenomena this master theses aims to study.

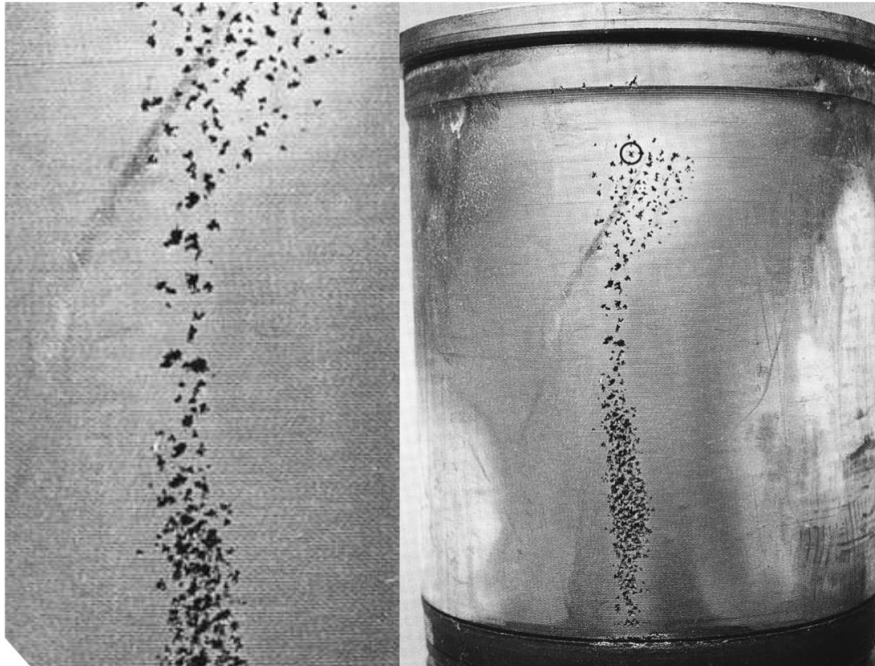


Figure 1.4: A cylinder liner where cavitation has occurred on the outer wall.

1.3 Simulation program

The simulation program is specifically designed to calculate the piston secondary motion, forces, and displacements within a PCU. The program also takes the influence of the lubrication oil distribution into account, as mentioned earlier. The inputs that are needed are supplied in .txt-format and describe the geometry of the piston, how it behaves when loads are applied, but also the temperature of the lubrication oil depending on where in the combustion cycle the piston is located. In addition to this data such as mass and mass moment of inertia, as well as data regarding the viscosity of the oil and initial oil film thicknesses have to be defined. The details of this can be read more about in Section 2.

1.4 Previous work

In Totaro's study [3] the influence of different geometric patterns on the piston skirt was studied, and it was shown that great differences in friction could be seen due to the variations in hydrodynamic pressure between the different designs.

Studies regarding piston secondary motion and the friction in power cylinder units have been done previously, as for example in *The Effects of Piston Skirt Profiles on Secondary Motion and Friction* by O. Akalin and O. Gunelsu [2] and *Technique of Measuring Piston Secondary Motion Using Laser Displacement Sensors* by Z.M. Ripin and Y-C. Tan [4].

1.5 Purpose

The primary goal is to compare two different piston types, *Piston A* and *Piston B*, with respect to piston skirt friction, piston secondary motion, lubrication oil distribution, and pressure on the cylinder liner.

Furthermore, another goal is to help Volvo create a methodology and tutorial regarding how to obtain input data and running the program which can be used by Volvo in future work with their power cylinder units.

Another goal is to perform a parametric study to investigate the influence certain parameters have on the piston secondary motion, skirt friction, and so on.

Lastly, to aid the developers in the development of the software, the purpose of this project is also to report areas of improvement regarding the program, and to make the developer aware of bugs and other errors.

1.6 Scope and limitations

In order to keep the work focused and within clearly defined framework, certain limitations have to be implemented.

- The simulations to obtain forces, displacements, pressures, and lubrication oil distribution will be carried out with the software.
- Only two different pistons are analyzed, i.e. two different power cylinder units are considered.
- Only the second of the four lands will be taken into account in the analyzes.
- The computational work for obtaining the piston and cylinder liner compliance and node positional data will be performed by a simulation engineer at Volvo with recommendations from the authors regarding how the information should be saved and any adjustments that need to be made for the geometry of the parts included in the power cylinder unit.
- Thermal deformations and temperatures have not been calculated during the project. Existing data has been used which are not produced for the same, but similar, operating conditions.

2

Modeling of the piston secondary motion

In this chapter the most important pieces of the theory behind the simulation software, such as the dynamics and kinematics of the piston, the hydrodynamic model, as well as the contact model will be presented.

2.1 The piston primary and secondary motion

The piston primary motion is the motion of the piston aligned with the cylinder liner's longitudinal axis, see Figure 2.1. If the piston motion is modelled in this idealized way, the piston has only one degree of freedom. The piston secondary motion is the deviating motion of the piston from the cylinder's longitudinal axis (Figure 2.1). It can be decomposed into a motion perpendicular to the longitudinal cylinder axis (piston lateral motion - a pure translation) and a rotation around the wrist pin (piston tilting motion - a pure rotation). Thus, the piston secondary motion accounts to two degrees of freedom, the lateral motion in the y-direction and the rotation about the x-axis (see Figure 2.1, as the lateral motion in the x-direction and the rotation about the y-axis are considered to be significantly lower).

As mentioned in Section 1.2 the driving force in the piston cylinder unit is the combustion force (also referred to as combustion chamber pressure). This force drives the piston primary motion.

The resulting reaction force arises due to the connecting rod angle, the possible piston tilt angle, as well as the inertia of the components in the power cylinder unit, and the combustion pressure not being perfectly uniformly distributed. Thus, the resulting reacting force is the sum of several forces. Furthermore, if the net moment of these forces is nonzero, the net moment entails the piston angular acceleration around the piston's wrist pin. It is the resulting reaction force and the angular acceleration of the piston which drives the piston secondary motion. If the engine runs with constant RPM (Revolutions Per Minute), the piston secondary motion tends to come into contact with the cylinder liner at the same location every combustion cycle the piston makes. This special tendency is empirically known and is important for the cavitation phenomenon.

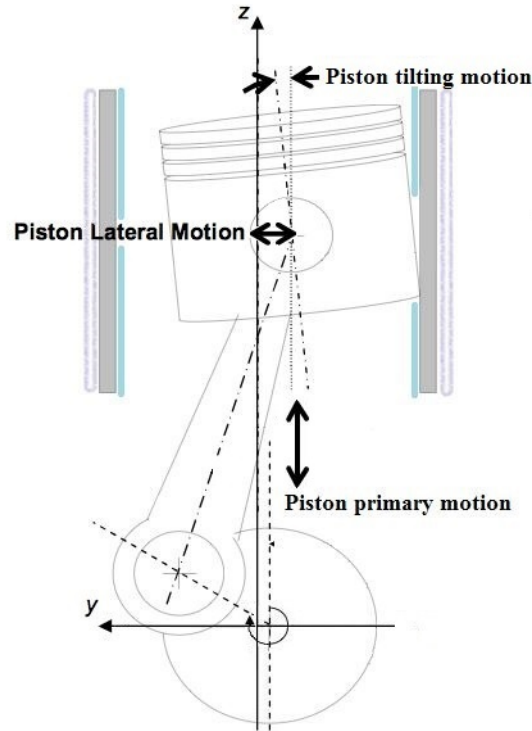


Figure 2.1: The piston primary and secondary motion. The piston primary motion can be seen as the remaining motion if one omits the piston lateral motion and piston tilting motion, i.e. the piston secondary motion.

2.2 Physical models

The governing equations in the software consist of kinematic and dynamic relations as well as a hydrodynamic model. These together describe how the piston interacts with the cylinder liner and how the oil-film is distributed in the power cylinder unit. The coordinate system is defined as in Figure 2.1, with its center in the crankshaft axis and with the x-axis perpendicular to the y- and z-axis, directed into the paper. The piston primary motion decides the instantaneous piston sliding speed in the cylinder liner and is an important parameter for the calculation of the lubricant oil-film distribution. Thus, the piston primary motion is needed in the hydrodynamic model presented in Section 2.2.2.

2.2.1 Dynamics and kinematics

The understanding of the interaction between the piston and the cylinder liner is necessary since that interaction is related to the resulting reaction force which contributes to the piston secondary motion. In this section the conclusive equation is explained in order for a better understanding. The full derivation and all the explicit equations can be found in *Modelling Piston Skirt Lubrication in Internal Combustion Engines* [5].

Force balance

Firstly, the force balance in the x-direction is omitted because the movement of the piston in the x-direction is significantly smaller than the movement of the piston in the y-direction. When the piston secondary motion is mentioned in this thesis, it always refers to the piston's lateral movement in the y-direction and the tilting around its x-axis. Secondly, the force balance in the z-direction is only needed in order to find the z-components which is added to the force balance in the y-direction, due to the piston tilt, ϕ . Of that reason, the force balance in the z-direction is not brought up here, but is involved indirectly in the conclusive equation for the force balance in the y-direction and in the conclusive equations for the moment balance.

According to the thesis of Bai, D. [5] the force balance in the y-direction for piston-cylinder liner interaction is given by

$$F_{y_{cb}} + F_{y_{wp2ps}} + F_{y_p} - m_{ps}a_{py} = 0 \quad (2.1)$$

which is the so called conclusive force balance equation and is programmed into the software. Equation (2.1) is visualized in Figure 2.2. The term m_{ps} is the mass of

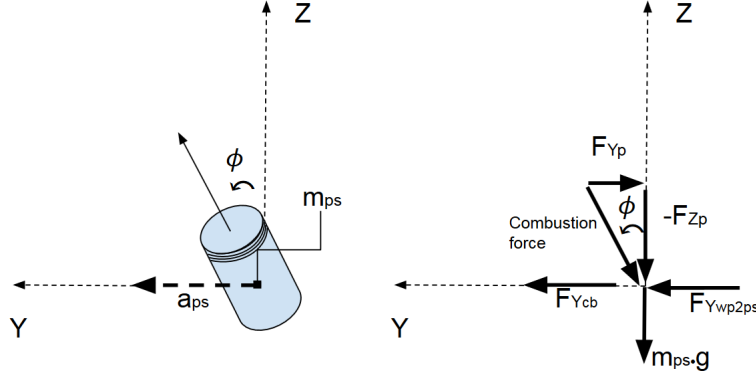


Figure 2.2: Free body diagram of the piston with tilting angle ϕ .

the piston and a_{py} is the acceleration of the piston in the y-direction. $F_{y_{cb}}$ is the resulting reaction force from the piston-cylinder liner interaction and is unknown. F_{y_p} is given by

$$F_{y_p} = -F_{z_p} \tan(\phi) \quad (2.2)$$

and describes the lateral component of the combustion force due to the piston tilting angle ϕ . The variables ϕ and a_{py} are directly related to the piston secondary motion. $F_{y_{wp2ps}}$ is a large component with respect to the number of terms it contains but it merely describes the lateral force in y-direction that acts on the piston from the wrist pin. $F_{y_{wp2ps}}$ is the primary force which drives the piston lateral motion and is

2. Modeling of the piston secondary motion

explicitly given by

$$\begin{aligned}
 F_{y_{wp2ps}} = & \left(- \underbrace{\frac{L_{CR} \cdot \sin(\beta) \cdot F_{z_{wp2cr}}}{L_{CR} \cdot \cos(\beta)}}_{=(\#1)} - \underbrace{\frac{Y_{crcg/Q} \cdot m_{cr} \cdot a_{crcgz}}{L_{CR} \cdot \cos(\beta)}}_{=(\#2)} + \dots \right. \\
 & + \underbrace{\frac{Z_{crcg/Q} \cdot m_{cr} \cdot a_{crcgy}}{L_{CR} \cdot \cos(\beta)}}_{=(\#3)} - \underbrace{\frac{I_{cr} \cdot \ddot{\beta}}{L_{CR} \cdot \cos(\beta)}}_{=(\#4)} + \dots \quad (2.3) \\
 & \left. - \underbrace{m_{wp} \cdot a_{py}}_{=(\#5)} \right)
 \end{aligned}$$

The term (#1) corresponds to the force from the connecting-rod to the wrist pin. (#2) and (#3) are the forces due to the acceleration of the connecting-rod in the y and z-direction, respectively, with respect to the center of gravity of the connecting-rod. (#4) is the force of the connecting rod due to the angular momentum of the connecting-rod around its center of gravity. (#5) corresponds to the force of the wrist pin acting on the piston. L_{CR} is the length of the connecting-rod and β is the angle between the connecting-rod and the z axis. $Y_{crcg/Q}$ and $Z_{crcg/Q}$ is the length from connecting-rod to arbitrary point Q when $\beta \neq 0$, in the y- and z-direction respectively, with respect to the connecting-rod's center of gravity. m_{wp} and m_{cr} is the mass of the wrist pin and connecting-rod, respectively, and I_{cr} is moment of inertia of the connecting-rod.

For an explanation of the individual variables in Equation (2.3) consult Table A.1.

Moment balance

The moment balance for the piston relative to its center of gravity is derived from

$$T_{ps} = I_{ps} \cdot \ddot{\phi} \quad (2.4)$$

where the term T_{ps} is given by

$$T_{ps} = F_{y_{wp2ps}} \cdot Z_{psc/P} - F_{z_{wp2ps}} \cdot Y_{psc/P} + T_{pcom} + T_{cb} \quad (2.5)$$

The terms $F_{y_{wp2ps}}$ and $F_{z_{wp2ps}}$ are the forces from the wrist pin acting on the piston. T_{pcom} is the moment due to the combustion chamber pressure. T_{cb} is the moment from the interaction between the piston and the cylinder liner. The remaining variables in equation (2.5) are distances, and for an explanation of these, consult Table A.1. Expressing Equation (2.4) as

$$F_{y_{wp2ps}} \cdot Z_{psc/P} - F_{z_{wp2ps}} \cdot Y_{psc/P} + T_{pcom} + T_{cb} - I_{ps} \cdot \ddot{\phi} = 0 \quad (2.6)$$

gives the so called conclusive moment equation which is programmed into P2M.

2.2.2 Hydrodynamic model for the lubrication oil-film

Navier-Stokes Equation (NS)

The hydrodynamical model in the simulation software is based on Navier-Stokes equation

$$\underbrace{\frac{\partial \rho u_i}{\partial t}}_{\text{The material derivative}} + \underbrace{\frac{\partial \rho u_i u_j}{\partial x_j}}_{\text{Convection term}} = \underbrace{\frac{\partial \tau_{ij}}{\partial x_j}}_{\text{The deviatoric stress tensor}} - \underbrace{\frac{\partial p}{\partial x_i}}_{\text{Hydrostatic pressure}} \quad (2.7)$$

and the continuity equation

$$\frac{\partial \rho}{\partial t} + \nabla_i u_i = \Phi \quad (2.8)$$

because the lubrication oil is assumed a incompressible fluid. ρ denotes the density of the fluid, t the time, u the flux of the lubrication oil, Φ the generation of lubrication oil per unit time and p the pressure. Navier-Stokes equation correspond to the conservation law of momentum of the viscous substance and the equation of continuity states that the mass must be conserved. In this case the viscous substance is the lubrication oil between the piston and the cylinder liner. The Navier-Stokes and continuity equation is written with index notation, which basically means that Navier-Stokes equation corresponds to three equations, depending on how many coordinate axes that are needed in order to express the problem. Thus, these four equations (three NS-equations and one continuity equation) have to be solved simultaneously and are heavy from a computational point of view due to the fact that a fine mesh is needed in order to capture the behavior of the oil distribution, and because of the intrinsic property, that the general form of Navier-Stokes equation, in fact, corresponds to three equations.

Reynolds equation

In order to make the simulation time reasonable Navier-Stokes equation and the continuity equation is used together and simplified to the Reynolds equation

$$\underbrace{\frac{\partial}{\partial x} \left(\frac{h^3}{12\mu} \frac{\partial p}{\partial x} \right) + \frac{\partial}{\partial z} \left(\frac{h^3}{12\mu} \frac{\partial p}{\partial z} \right)}_{\text{Poiseuille flow}} = \underbrace{\frac{U}{2} \frac{\partial h}{\partial z}}_{\text{Couette flow (Shear driven flow)}} + \frac{\partial h}{\partial t} \quad (2.9)$$

where x denotes the circumferential direction and z the centerline axis of the cylinder liner, according to Figure 2.1. h denotes the clearance between the piston skirt, piston land and the cylinder liner, and μ is the dynamic viscosity of the lubricant. U is the piston sliding speed along the z -direction.

Assumptions are made that the oil is a *Newtonian fluid*, the inertia and gravity of the oil are neglectable and that the oil can not slip on the solid surfaces, i.e on the piston skirt, piston land or the cylinder liner. Lastly, the oil-film is also assumed to be thin in comparison to its vertical distribution. The assumption that the lubrication oil is considered as a *Newtonian fluid* means that the viscous stresses in the oil

2. Modeling of the piston secondary motion

is linearly proportional to the strain rate in the oil, over time, and continuously throughout the oil. Of these assumptions the most important one is that the oil-film is thin compared to its vertical distribution, which makes it possible to neglect the pressure gradient in the radial direction in the oil-film [5, p. 49]. With these six assumptions Navier-Stokes equation (2.7) is simplified to Reynolds equation (2.9) which is programmed into the software.

Cavitation

Cavitation may occur when the pressure in the oil film between the piston skirt and the cylinder liner drops beneath the cavitation pressure of the oil for the current temperature. This may happen as consequence of the piston secondary motion due to rapid changes of the pressure. When the oil pressure drops beneath the cavitation pressure of the oil, the lubricating oil cavitate and a void is created filled with oil vapor and dissolved gas. The cavitation phenomenon is very complex and this master thesis does not take the wear due to cavitation into account, but there is a possibility that the simulations will show locations in the oil-film between the piston skirt and the cylinder liner where cavitation has occurred.

Universal Reynolds equation

Reynolds equation (2.9) is only valid in the region where no cavitation occurs. This is because where cavitation occurs there is no pressure gradients, and hence no Poiseuille flow. Thus, it is important to know in which regions the Reynolds equation can be used and what to do in the other regions, to get accurate results. This means that Reynolds equation according to Equation (2.9) is not enough in its current form for the software in order to get a realistic description of the lubrication oil distribution.

The Jakobson-Floberg-Olsson (JFO) theory suggests that the lubrication oil field can be divided into two different regions. The region where the cavitation occurs is called the partial film region due to that the region is only partially filled with oil. The other region is called the full film region and is, instead, filled with oil. Thus, until now, it is only in the full film region that the Reynolds equation is valid. When taking the cavitation phenomena into account the hydrodynamic model becomes significantly more complex than before because it results in two different regions where two different governing equations rule.

In order to obtain two different functioning governing equations the first difficulty is how to decide which regions that are partial film regions, and which are full film regions. Cavitation occurs when the hydrodynamic pressure p drops below cavitation pressure, and thus defines the partial film region. But the hydrodynamic pressure is in fact one of the unknowns that the software is trying to solve for. The second difficulty is that the unknown variables are different in different regions. In the full film region the hydrodynamic pressure p is unknown. In the partial film region p is the cavitation pressure (which is known) but instead the density ρ is unknown. Thus p and ρ are only valid locally and this difficulty is solved by introducing two new variables, F' and Φ , that have different significance depending on if the partial film region or the full film region are considered. These global variables are defined

as

$$\begin{cases} p = F' \Phi P_{ref} \\ \rho = [1 + (1 - F') \Phi] \rho_{ref} \end{cases} \quad (2.10)$$

where P_{ref} is a scaling factor for the hydrodynamic pressure and is set to 1 bar and ρ_{ref} is the lubricant oil density. F' changes depending on the partial film region ($F' = 0$) or the full film region ($F' = 1$). Φ represents the pressure if $F' = 1$ and the oil-distribution ratio if $F' = 0$. Thus, the new variables F' and Φ are valid globally and describe which oil-film region that is currently active.

Inserting the global variables (2.10) into Reynolds equation (2.9) in this specific way gives the final governing equation for the hydrodynamic model. Namely, the Universal Reynolds equation according to

$$\begin{aligned} \frac{\partial}{\partial x} \left(\frac{h^3}{12\mu} \frac{\partial(F' \Phi P_{ref})}{\partial x} \right) + \frac{\partial}{\partial z} \left(\frac{h^3}{12\mu} \frac{\partial(F' \Phi P_{ref})}{\partial z} \right) = \dots \\ \frac{U}{2} \frac{\partial}{\partial z} \{ [(1 + (1 - F') \Phi) \rho_{ref}] h \} + \frac{\partial}{\partial t} \{ [(1 + (1 - F') \Phi) \rho_{ref}] h \} \end{aligned} \quad (2.11)$$

and how this is done can be read about in *Modeling Piston Skirt Lubrication in Internal Combustion Engines* [5].

2.3 Contact model

Asperity contact means solid-to-solid contact and must be modelled after how the geometries of surfaces of the piston skirt and cylinder liner look. When looking at the asperity contact in the model, the tooling marks in the piston skirt surfaces have to be taken into consideration.

The tooling marks of the piston skirts are of triangular shape, and are generally significantly longer than they are high, meaning that the wave length is greater than the wave height. Figure 2.3 shows schematically how the tooling marks look. With

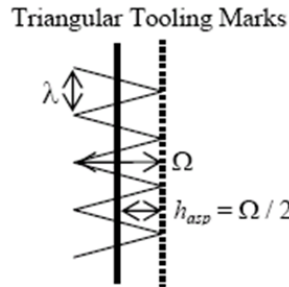


Figure 2.3: The model of tooling marks on the piston skirts, taken from [1].

this assumption made, the software uses the analytical solution for a blunt wedge against a plane, which was developed by Johnson [6].

2. Modeling of the piston secondary motion

The asperity height h_{asp} is defined as half the wave height of the tooling marks, and h is defined as the gap between the cylinder liner and the centerline of the piston skirt surface. The asperity pressure is then calculated by

$$P_{asp} = \begin{cases} A_1 \delta^{A_2}, & h < h_{asp} \\ 0, & h \geq h_{asp} \end{cases}$$

where $\delta = h_{asp} - h$, and the constants A_1 and A_2 are calculated by the software, assuming the wave length λ , wave height Ω , and material parameter E have been used as input [1]. The parameter E is defined as

$$E = \left(\frac{1 - \nu_1^2}{E_1} + \frac{1 - \nu_2^2}{E_2} \right)^{-1} \quad (2.12)$$

where E_i and ν_i are the Young's moduli and Poisson's ratios for the materials in contact, respectively. I.e. E is used when asperity contact is reached.

2.4 Globally convergent Newton's method

Table 2.1 shows the unknown variables in Equation (2.1) and (2.6). All other parameters in Equation (2.1) and (2.6) are known for every given crank-angle. ϕ and a_{py} correspond to the parameters which influence the piston secondary motion. $F_{y_{cb}}$ is solved after the hydrodynamic model has been solved and is the resulting net force from the asperity contact and the pressure distribution in the lubrication oil which has been calculated in the software with the hydrodynamic model. These three terms are solved iteratively in the software.

Table 2.1: Unknown variables in the conclusive Equations (2.1) and (2.6).

ϕ	[rad]	The piston tilting angle.
a_{py}	[m·s ⁻²]	The acceleration of piston in the y-direction
$F_{y_{cb}}$	[N]	The resulting friction force between the piston and the cylinder liner.

In order to solve the unknowns according to Table 2.1, the software uses a globally convergent Newton's method, which is an iterative method for solving equation systems. Basically, Newton's method solves the equation system approximately, referred to as the *function vector* in this context, until the norm of the residuals for every element in the function vector are smaller than some predefined tolerance for every corresponding element. The function vector contain, among others, the unknown variables according to Table 2.1 and is defined as

$$\mathbf{X} = \begin{bmatrix} F_{y_{cb}} + F_{y_{wp2ps}} + F_{y_p} - m_{ps}a_{py} \\ V_{py}^i - \frac{x_{py}^i - x_{py}^{i-1}}{\Delta t} \\ F_{y_{wp2ps}}Z_{pscg/P} - F_{z_{wp2ps}}Y_{pscg/P}Y_{pscg/P} \quad \dots \\ + T_{pcom} + T_{cb} - I_{ps}\ddot{\phi} \\ \dot{\phi}^i - \frac{\phi^i - \phi^{i-1}}{\Delta t} \\ CF_0^1 - d_0^1 \\ CF_0^2 - d_0^2 \\ \vdots \\ CF_0^i - d_0^i \end{bmatrix}^T \quad (2.13)$$

The other equations in (2.13) correspond to the piston's lateral velocity in the y-direction (row two), piston angular velocity (row four) and the error in deformation ($CF_0^1 - d_0^1$ to $CF_0^i - d_0^i$) for each node i (the higher indice). All of these equations are stated in a function vector \mathbf{X} , as mentioned earlier, in order to use Newton's method. d_0 is the assumed initial guess of deformation, F_0 the calculated force field and C the compliance matrix. Thus $CF_0^1 - d_0^1$ to $CF_0^i - d_0^i$ specifies the error in deformation for every node i.

The reason why the norm of the residual for every element are compared to a predefined tolerance value of its own, is because it is not realistic that Newtons method should be able to converge when the norm of all the elements in the function vector is small enough, except for one element (e.g. $\mathbf{X}(2)$) where the value is too big. If so, the solution would be unphysical and uninterpretable.

In the beginning, Newton's method tries to solve the function vector (2.13) from an initial guess. If no solution is found (this is generally always the case for the initial guess) Newton's method uses the new calculation as a new guess, and calculates the norm of the new residuals for all the elements in the function vector and compare these to the predefined tolerances for the corresponding elements of the function vector. The process is repeated iteratively until all the norms are smaller than all the predefined tolerances. This is done for every crank angle step until the simulation is done.

2.5 Assumptions and simplifications

For the kinematic and dynamic theory, and the hydrodynamic model, the following assumptions and simplifications according to Table 2.2 have been made in order to make the derivations more manageable.

The purpose of Table 2.2 is to summarize the assumptions, simplifications and

2. Modeling of the piston secondary motion

limits that were mentioned earlier as well as clarify ones that were only stated in a short manner, so that all of them can be found at the same location in this report.

Table 2.2: Assumptions and simplifications related to the theory.

Area	Assumption or simplification
Kinematics and dynamics	Only three degrees of freedom of the motion of the piston are considered, which are: The piston primary motion (one degree of freedom), the piston secondary motion (two degrees of freedom). The three remaining ones are assumed to be insignificant compared to the piston primary and secondary motion and are neglected.
Kinematics and dynamics	The force from the combustion pressure is assumed to be uniformly distributed.
Kinematics and dynamics	The connection between connecting rod and crankshaft is considered frictionless.
Kinematics and dynamics	The connections between wrist pin and piston and between the wrist pin and connecting rod are considered frictionless.
Kinematics and dynamics	The connecting rod, wrist pin, and piston are considered rigid with distributed mass.
Hydrodynamic model	The oil in the power cylinder unit is assumed to be a Newtonian fluid.
Hydrodynamic model	The inertia and body forces of the oil are neglected.
Hydrodynamic model	The oil is assumed to be incompressible.
Hydrodynamic model	It is assumed that the oil can not slip on the surfaces of the piston and on the cylinder liner.
Hydrodynamic model	The thickness of the oil is assumed to be thin in comparison to the lateral size of the piston.

2. Modeling of the piston secondary motion

3

Obtaining input data

To run the simulations certain input data is needed. This included geometry and compliance of both the piston skirt and the cylinder liner, geometry of tooling marks on the piston skirt, viscosity of the lubrication oil and constants for the viscosity model, initial oil film thickness in the power cylinder unit, as well as the overall geometry. How this information was obtained and implemented will be presented in this chapter. Additional data needed for the analyses is shown in Table 3.1. Some of these parameters have not been investigated in the cases of the specific power cylinder units, and have been determined by discussing with the software developers.

Table 3.1: The given data for the Piston A, Piston B, 10W-30 Oil and the initial oil values for the cylinder liner.

Friction coefficient during asperity contact	[-]	0.03
Oil-splash	[μm]	10
Film thickness during solid-to-solid contact	[μm]	0.5
Lubrication oil density (10W-30 oil)	[$\text{kg}\cdot\text{m}^3$]	850

3.1 Piston geometry

The main measurements of the piston geometries were obtained by studying the blueprints of the concerned pistons. However, to describe the more intricate parts of the pistons that were needed as input, such as radial variation of the skirt and chamfer compared to the nominal radius, the manufacturer of the piston had to be contacted to get node positions that were detailed enough to describe the radial variation. Since these node positions did not lie on the same coordinates as the node positions that were used to obtain the piston compliance (see Section 3.3), the cold radial variation had to be mapped on to those nodes, which was done by interpolation.

3.1.1 Radial variation of pistons due to thermal effects

Due to the temperature increase of the pistons that occurs during operation, the pistons' geometry will change compared to the cold piston geometries. The ideal

3. Obtaining input data

information regarding how the pistons expand would be to carry out a finite element analysis with proper boundary conditions applied to get a geometry change close to reality. However, since such data was not available, the radial change of the pistons due to thermal effects were obtained from data sheets supplied by the manufacturer that described how the pistons change shape when they operate. This data was limited with regard to how the pistons radial variation changes angularly, and as a result of this a simplification was made that the thermal effect is circularly uniform with regard to the pistons' Z-axis. How the geometries of the pistons look when the engine is operating, but with exaggerated radial variations, can be seen in Figure 3.1.

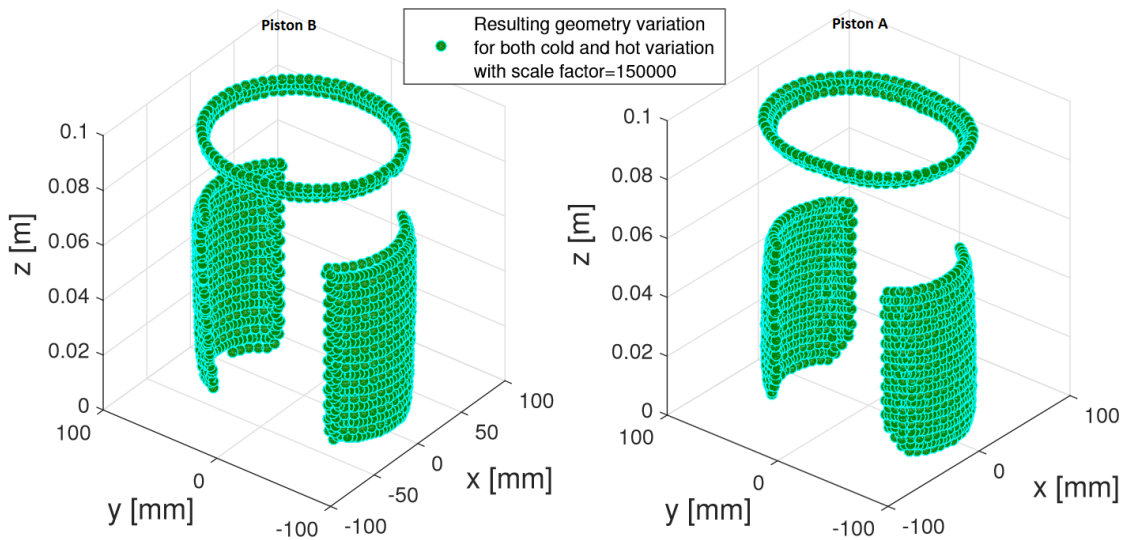


Figure 3.1: Geometry with exaggerated radial variations of Piston B and Piston A with both cold and hot variation taken into account.

3.2 Cylinder liner geometry

In the same manner as for the pistons, the geometry for the cylinder liner was attained by creating a grid from an existing CAD model and saving the node positions. However, the CAD model did not include the cylinder liner's cold radial variation and by that, the cold geometry of the cylinder liner was assumed to be perfectly cylindrical.

3.2.1 Radial variation of cylinder liner due to thermal effects

In the same way as for the pistons, the cylinder liner is affected by the heat that arises during the combustion cycle. Volvo could provide data that described the radial expansion due to assembly stresses and thermal effects at each vertical position in the cylinder liner. This meant that an assumption was made that the cylinder liner also expanded axisymmetrically with regard to the Z-axis.

3.3 Compliance

To simulate how the piston skirt, second land, and cylinder liner deforms due to mechanical loads, the compliance of the nodes describing these surfaces needed to be obtained.

$$\begin{bmatrix} \mathbf{K}_{bb} & \mathbf{K}_{bi} \\ \mathbf{K}_{ib} & \mathbf{K}_{ii} \end{bmatrix} \begin{bmatrix} \mathbf{u}_b \\ \mathbf{u}_i \end{bmatrix} = \begin{bmatrix} \mathbf{f}_b \\ 0 \end{bmatrix} \quad (3.1)$$

$$u_b = \underbrace{[\mathbf{K}_{bb} - \mathbf{K}_{ib}^T \mathbf{K}_{ii}^{-1} \mathbf{K}_{ib}]}_{\mathbf{C}_{bb}}^{-1} \mathbf{f}_b \quad (3.2)$$

To get hold of the compliance of the piston skirt and cylinder liner, the software requires information from an external finite element analysis. A mesh over the piston and cylinder liner was created. The compliance for the piston skirt, second land, and cylinder liner was obtained by applying a force of 1N in one node, normal to the surface, and recording the displacement of the nodes, i , on the skirt, second land and cylinder liner. This created one data set, and this method was then repeated i amount of times in order to record how the piston compliance responded for a force of 1N in every node. How this procedure is described in a mathematical way is described by equations 3.1 and 3.2.

The compliance is of course directly related to the boundary conditions. In the calculation of the compliance of the piston, due to the interaction with the cylinder liner, the nodes on the surface where the piston is in contact with the wrist pin were locked, shown in Figure 3.2.

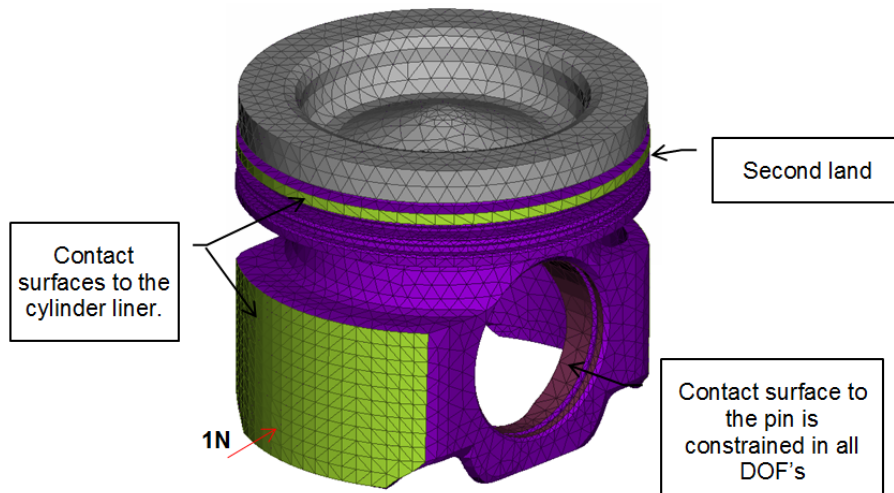


Figure 3.2: 1N is applied at each node on the second land of the piston and the piston skirt, one at a time, to obtain the piston compliance.

For the cylinder liner nodes located at the top of the cylinder were locked, namely the surface that is in contact with the cylinder block, with the normal of the surface

3. Obtaining input data

pointed in the negative z-direction. Figure 3.3 shows the cylinder liner where 1 N is applied to the nodes on the inside of the cylinder liner, and the surface of the cylinder liner, which were constrained in their degrees of freedom. The compliance

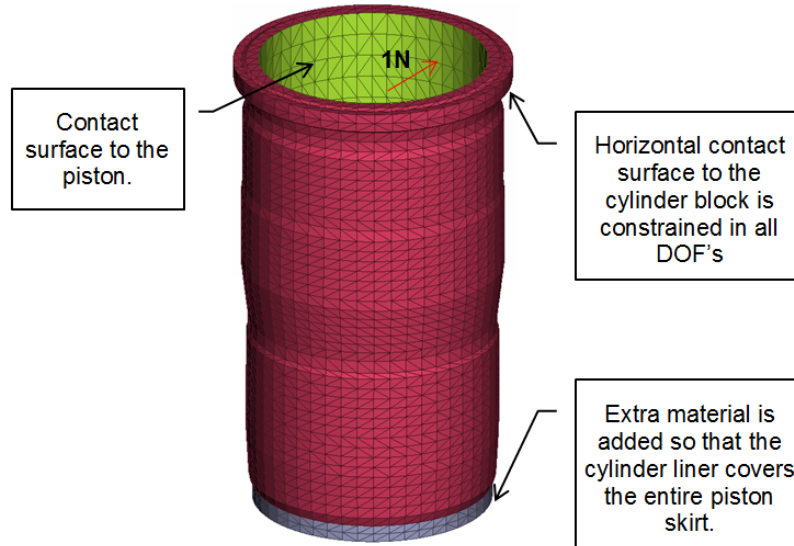


Figure 3.3: A figure of the cylinder liner showing the constrained surface, the applied load, and extended liner part.

of the piston due to combustion pressure was obtained by applying a uniformly distributed pressure of 1 bar on the piston top (see Figure 3.4) and measured the displacement of the nodes on the piston skirt and 2nd land. For that case, only a certain part of the nodes located on the surface that is in contact with the wrist pin had their degrees of freedom locked, see Figure 3.5.

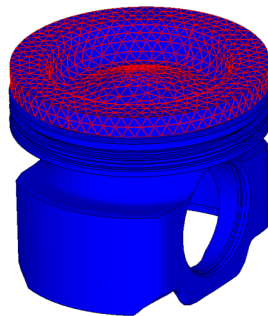


Figure 3.4: A uniformly distributed pressure of 1 bar on the piston top in order to obtain the piston compliance due to the combustion pressure.

The choice of locking the nodes of the piston where the wrist pin is attached when obtaining the compliance is a simplification compared to how the contact condition behaves in reality. In reality the wrist pin presses on the piston differently depending on if the piston is moving towards TDC or BDC, as well as towards the thrust- or anti-thrust side. To make a more realistic analysis one way to improve

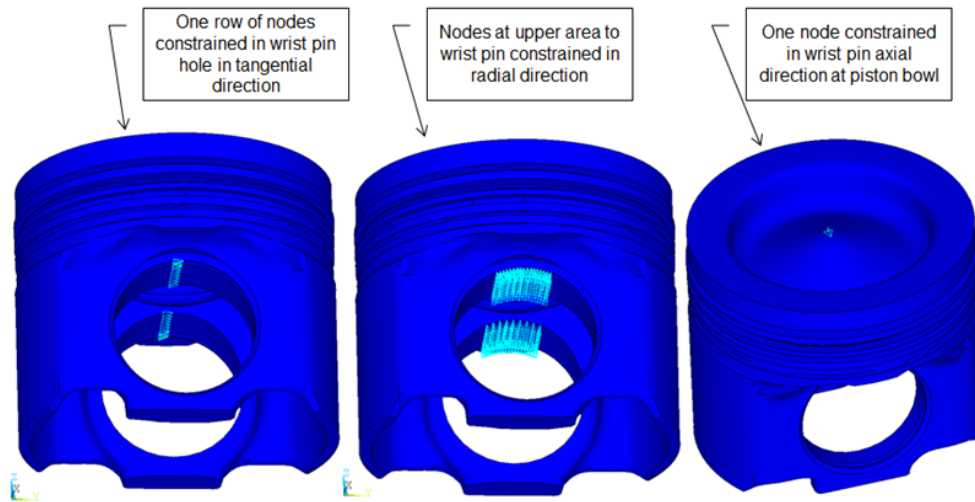


Figure 3.5: The boundary conditions of the piston when obtaining the compliance due to the combustion pressure.

the compliance modelling would be to carry out two different compliance analyzes: one where only the nodes on the upper half of the surface of the piston that is in contact with the wrist pin is locked, and one where the nodes on the bottom half of the surface are locked. Then, depending on if the wrist pin is pressing on the top or bottom half, a more realistic deformation shape of the piston during the entire cycle could be obtained. However, since the piston is affected by side forces as well, if an even more realistic analysis is wanted then that influence would have to be taken into consideration as well by changing the surface that is in contact depending on the direction of the resultant force. Even then, this very complex solution does not consider that the surface that is in contact between piston and wrist pin can change with applied loading. In reality it is reasonable to assume that the contact surface changes size depending on if a large or small force is applied.

3.4 Pressure data

The combustion pressure data used in the simulations had been obtained by a measurement carried out with a Piston B unit under steady state conditions for different revolution speeds at full load, which means that the RPM was constant during the measurements. It is assumed that the combustion pressure is the same for both pistons. The data was given as the pressure as a function of crank angle, covering one combustion cycle.

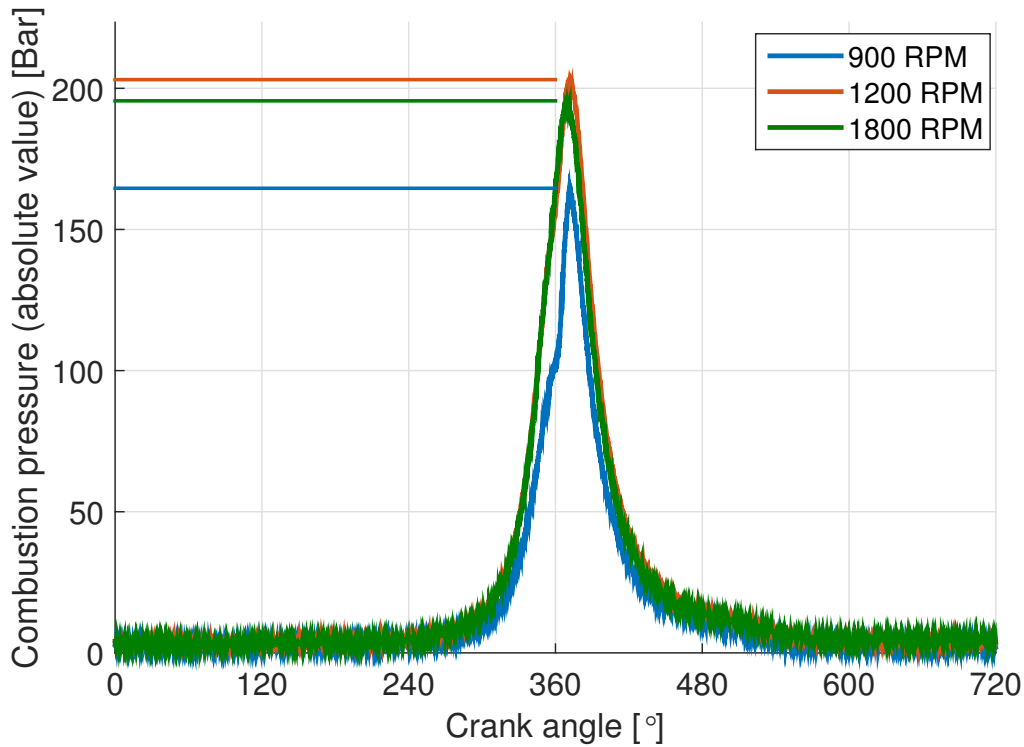


Figure 3.6: Given combustion pressures from Volvo for three different RPM-values measured under steady state conditions at full load.

3.5 Lubricating oil

3.5.1 Oil temperature

The temperature of the lubrication oil was calculated by taking the average temperature of the cylinder liner over the area that the piston skirt is currently covering. this temperature on the cylinder liner varies along the z-axis according to Figure 3.7. The temperature profile is calculated for steady state conditions. The cylinder liner is heated at the top where the combustion occurs at the same time as it is cooled further down. Even though the temperature of the cylinder liner reaches roughly 180°C at the top (Figure 3.7), the lubrication oil in the piston skirt contact will never obtain this temperature due to that the piston skirt never reaches equally high up as the piston top during the combustion cycle. The average temperature over the piston skirt can be seen in Figure 3.8.

The lubrication oil temperature that was used (see Figure 3.8) in the simulations, which was based purely on the cylinder liner's temperature, could be made more realistic if there is information available regarding the piston's temperature during operation. Rather than just using the cylinder liner's temperature an average temperature between the piston skirt and cylinder liner could be used. Assuming that the oil film thickness is sufficiently thin to obtain a homogenous temperature in the entire film this seems like an improvement compared to the currently used temperature for the lubrication oil. However, with the information available the chosen

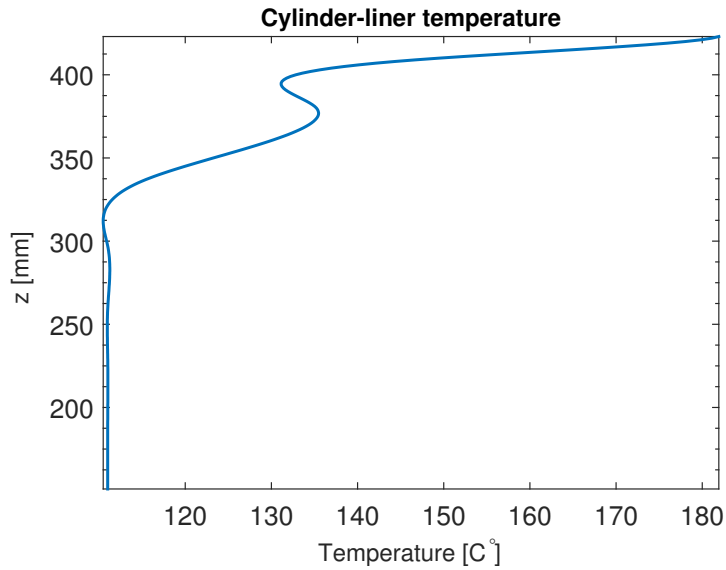


Figure 3.7: The temperature of the cylinder liner.

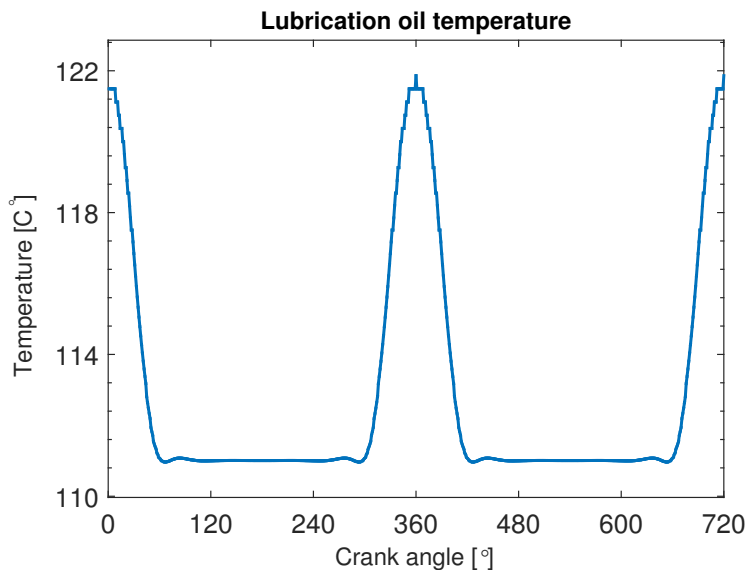


Figure 3.8: The temperature of the lubrication oil at the piston skirt over one combustion cycle.

method seems reasonable as the temperature of the piston skirt is not likely to vary significantly from the cylinder liner temperature.

3.5.2 Matching of viscosity models

The lubricating oil currently used by Volvo is a *10W-30 oil* which refers to a specific viscosity class for oils. The viscosity properties for the 10W-30 oil are shown in Table 3.2 for *shear rate* at 10^6s^{-1} .

3. Obtaining input data

Table 3.2: Dynamic viscosity for shear rate at 10^6s^{-1} for the 10W-30 oil.

Temperature [°C]	μ [mPa·s]
75	14.5029
100	8.0742
125	5.1589
150	3.6049

The model for the dynamic viscosity μ in the software is given by equation (3.3)

$$\mu(T, \gamma) = \underbrace{\overbrace{\kappa}^{=k \cdot \rho}}_{\mu_0} \cdot \exp\left(\frac{\theta_1}{\theta_2 + T}\right) \left(\frac{\mu_\infty}{\mu_0} + \frac{1 - \frac{\mu_\infty}{\mu_0}}{1 + \left| \frac{\gamma}{10^{(C_1 + C_2 T)}} \right|} \right) \quad (3.3)$$

and the model for the dynamic viscosity that Volvo uses is given by equation (3.4)

$$\mu(T, \gamma) = \underbrace{\rho k}_{\mu_0} \cdot \exp\left(\frac{\theta_1}{\theta_2 + T}\right) \left(\frac{1 + \frac{\mu_\infty}{\mu_0} \left(\frac{\gamma}{10^{(C_1 + C_2 T)}} \right)^m}{1 + \left(\frac{\gamma}{10^{(C_1 + C_2 T)}} \right)^m} \right)^{\nu_0} \quad (3.4)$$

θ_1 [°C], θ_2 [°C] and m [–] are correlation constants of the oil and ρ and T [°C], is the density and temperature of the oil. m is a correlation constant that takes the transition region from low-shear to high-shear viscosity, into account and controls the width of this region. γ [s^{-1}] is the shear rate and describes the rate at which shear rate deformation occurs in the oil.

Because the model for the dynamic viscosity built into the simulation software is different from Volvo's viscosity model, it was relevant to match the constants C_1 and C_2 to the ones described by the dynamic viscosity models which the software uses, so that the models coincides better. The matching was done computationally by minimizing the difference between the viscosity models with respect to C_1 and C_2 according to a least square fit method

$$\text{Min}_{C_1^{P2M}, C_2^{P2M}} \left(\begin{array}{c} [\text{Volvo's viscosity model}] (T, 10^6\text{s}^{-1}) \dots \\ - \dots \\ [\text{the software's viscosity model}] (T, 10^6\text{s}^{-1}) \end{array} \right) \quad (3.5)$$

That is, the difference between the models becomes as small as possible for a specific set of C_1 and C_2 for variable temperature T and constant shear rate γ . Furthermore, it was also relevant to quantitatively study how the optimized constants affected the models relative the given constants. This was done by computing the difference and the percentage change between the models with the calculated constants. The percentage change was computed according to equation (3.6).

$$\Delta = 100 * \frac{\left| [\text{Volvo's viscosity model}] - [\text{the software's viscosity model}] \right|}{\left| [\text{the software's viscosity model}] \right|} \quad (3.6)$$

Figure 3.9 shows the viscosity models before and after the matching and where the experimental values according Table 3.2 also can be seen. Due to that the difference between the models, both before and after the matching, is almost impossible to see in Figure 3.9, the absolute difference is plotted in Figure 3.10. The percentage change due to the matching can be seen in Figure 3.11.

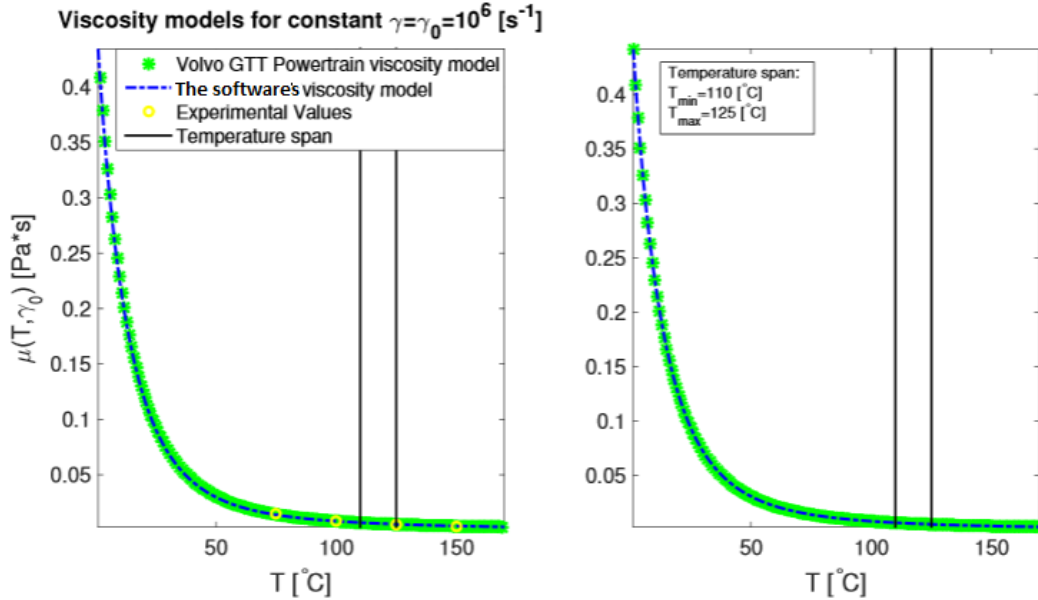


Figure 3.9: The dynamic viscosity according to Volvo’s viscosity model and the software’s viscosity model for varying temperature T . The left figure shows the models without matching and the right figure shows the models after matching. The temperature span refers to the temperature span for which the piston skirt is to be analyzed in, which means it’s the temperature spectrum where it is most important that the difference needs to be small. The experimental values refers to the values according Table 3.2.

Regarding the matching of viscosity models (3.3) and (3.4), there are a couple things to improve. Firstly, instead of matching with respect to a fixed shear rate, a matching over both the shear rate range and temperature range is likely to give more accurate results regarding the lubrication oil distribution. However, that requires a study where it is investigated what shear rate values the lubrication oil normally operates in, and minimize the error with regard to that range.

3. Obtaining input data

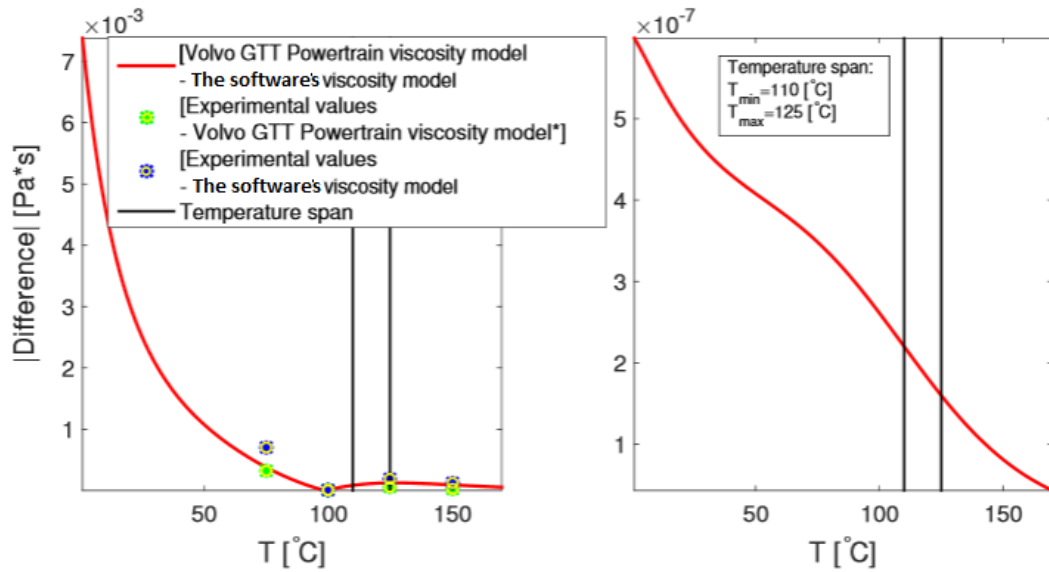


Figure 3.10: The difference between Volvo’s viscosity model and the software’s viscosity model before and after matching of the constants. The temperature span is defined as in Figure 3.9. The experimental values refer to the values according Table 3.2.

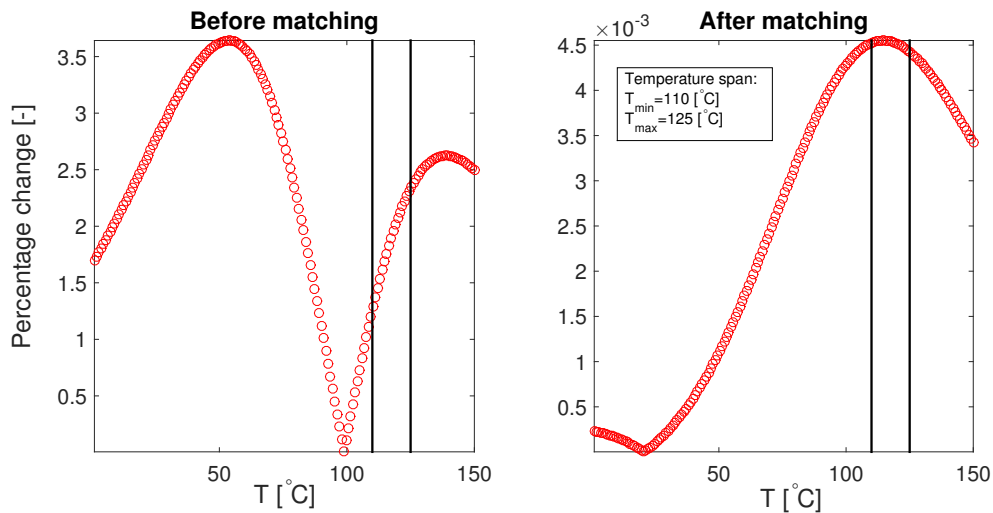


Figure 3.11: The percentage change between the two viscosity models before and after the matching of the constants.

3.6 Coating material

The coating material influences the input parameters in mainly two ways: the geometry of the tooling marks and the Young's Modulus needed to calculate the asperity contact. After discussions with the developers at MIT it was advised to not change the original tooling marks due to the coating material. However, when calculating the Young's modulus needed for the asperity contact equations, the modulus for the coating material was used instead of that of the piston material.

3. Obtaining input data

4

Results

This chapter is divided into four parts. The first part presents results regarding how simulation results vary from cycle-to-cycle and how that influenced succeeding simulations. The second and third part present the results from the simulations regarding the pistons A and B, respectively. The fourth, and last, part will show results for parameterizations with regard to rpm, combustion pressure, and oil splash, as these parameters vary during service. Increased rpm and combustion pressure is expected to give larger secondary motions and forces, while the expected influence of increased oil in the power cylinder unit is not as clear.

4.1 Cycle-to-cycle analysis

This section aims to show how the simulations vary on a cycle-to-cycle basis. The results shown in this section are from a simulation that has run for 2880 CA, or four combustion cycles, and were carried out for an early version of the piston B model.

As can be seen in Figure 4.1 the piston behaves roughly the same each combustion cycle. The peaks and valleys occur at the same places for all three graphs, and the magnitudes are very similar. This behavior is found for all results that can be visualized in a 2D-graph, such as asperity contact force, hydrodynamic force, friction force, and loss in power and energy due to friction.

Looking at Figure 4.2 the difference between successive cycles is visualized. For all three graphs it is apparent that the difference is the largest between the first and the second cycle, whereas the following cycles differ little in comparison. In all graphs it is apparent that the difference between the second and first combustion cycle (blue line) is large in the beginning of the cycle. This is due to the plotted quantity starting at 0 at the beginning of the simulations, and therefore not corresponding to its natural movement. Also, in the graph for the total side force exerted on the wrist-pin it looks as if the difference between the second and first combustion cycle varies a lot in the area around 380 degrees on the crank angle. This is due to the large derivatives found in the corresponding plot in Figure 4.1 and a small phase shift between the first and second combustion cycle. This behavior is not seen to the same extent in the comparison for the following combustion cycles, and together with the fact that the quantities not behaving in their real manner at the start of the simulation, it can be concluded that when looking at results the first combustion cycle should be discarded, and that the following combustion cycles behave in practically the same way. By this reasoning, when data regarding piston secondary motion, asperity contact, friction force, and so on, is presented, only data

4. Results

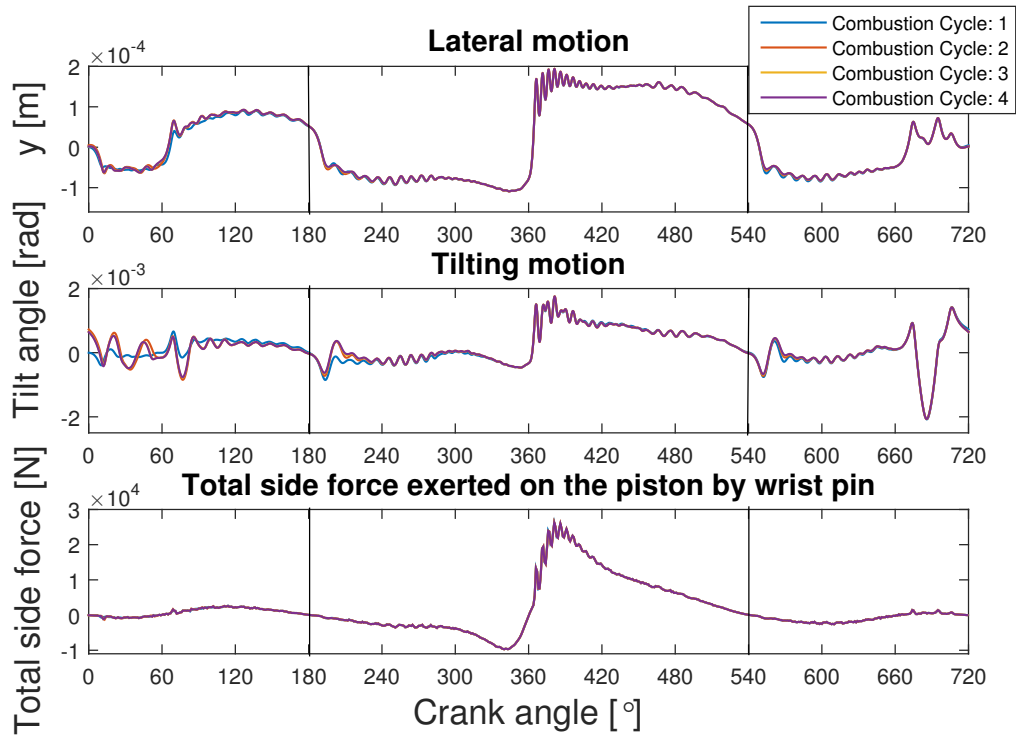


Figure 4.1: Cycle-to-cycle for lateral motion y , tilting angle ϕ , and the force $F_{y_{wp2ps}}$ acting on the piston B from the wrist-pin.

corresponding to the second combustion cycle is shown.

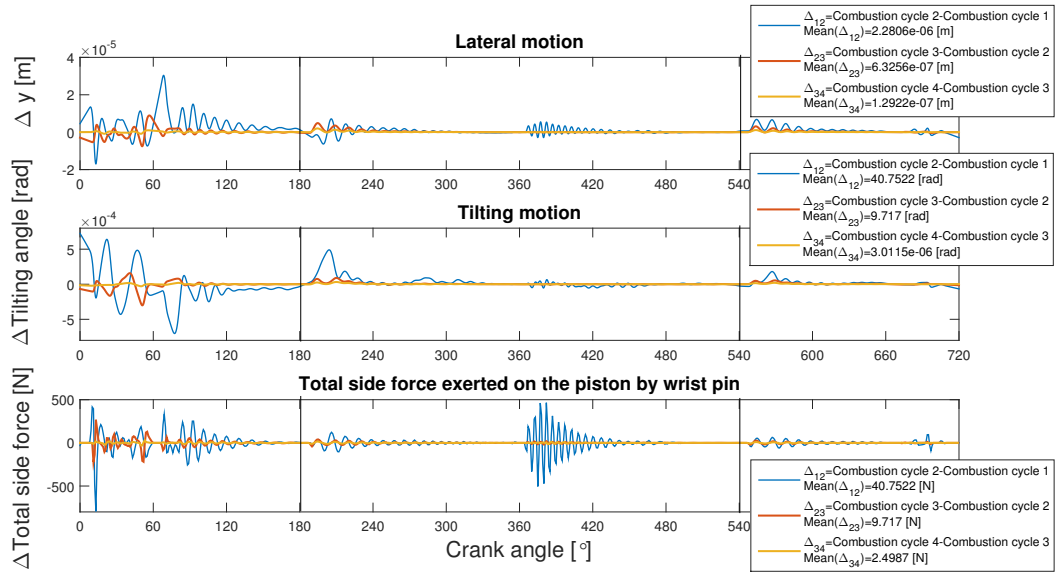


Figure 4.2: Differences and meanvalues between the four combustion cycles for lateral motion y , tilting angle ϕ , and force F_{ywp2ps} acting on the piston B from the wrist-pin.

4.2 Piston A

The following results for the piston A simulation correspond to a engine speed of 1200 rpm and just over 200 bar of peak combustion pressure.

4.2.1 Piston secondary motion and general forces

By observing the lateral motion of Piston A in Figure 4.3 a couple of interesting peaks can be found. Most notably there is a large peak present at around 400 degrees rotation of the crank shaft. The start of the peak corresponds to the point where the combustion pressure starts acting on the piston towards the thrust side, and its maximum lateral position of 150 μm is reached at roughly 480 degrees towards the thrust side. Aside from this large peak there are three other interesting areas seen during the combustion cycle; at around 120 degrees a peak is found, where the piston is pushed towards the thrust side, and between largest peak and the first peak there is an area where the piston is located towards the anti-thrust side. Then, after the combustion pressure has acted and the piston has passed BDC again, the piston is pushed towards the anti-thrust side again but is moving towards the cylinder's centerline axis.

In general the direction of which the piston is moved laterally correlates to which direction the connecting rod is leaning. During the first downstroke the connecting rod is leaning towards the thrust side, and as can be seen in Figure 4.3, the majority of the lateral motion of the piston during this period is directed towards the thrust side. For the subsequent upstroke, when the connecting rod is directed towards the anti-thrust side, the piston is located towards the anti-thrust side during the entire stroke. This behavior is also seen for the combustion cycle where the lateral position

4. Results

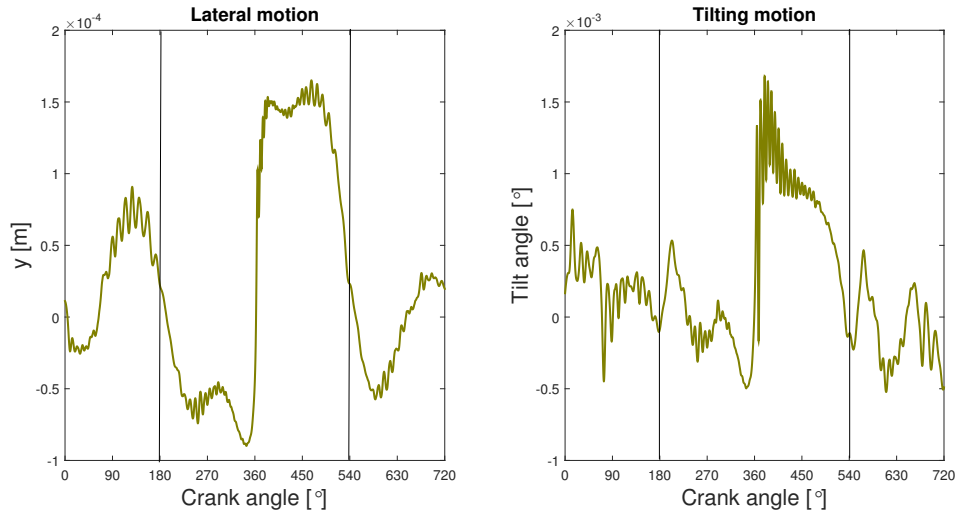


Figure 4.3: Lateral and tilting motion for the piston A during the second combustion cycle.

of the piston switches from thrust to anti-thrust side depending on the direction of the connecting rod during the cycle. The influence of the direction of which the connecting rod is leaning can also be seen in Figure 4.5 by observing the plot for the total side force exerted on the piston by the wrist pin. In the same way as for the lateral motion the total side force exerted on the piston by the wrist pin changes sign depending on if the piston is on a downstroke or upstroke.

For the tilting motion it is difficult to see any clear patterns or correlations except that the tilting angle is heavily influenced by the combustion pressure. As the combustion pressure acts on the piston the piston gets tilted significantly in a clockwise direction that is sustained for almost the entire downstroke.

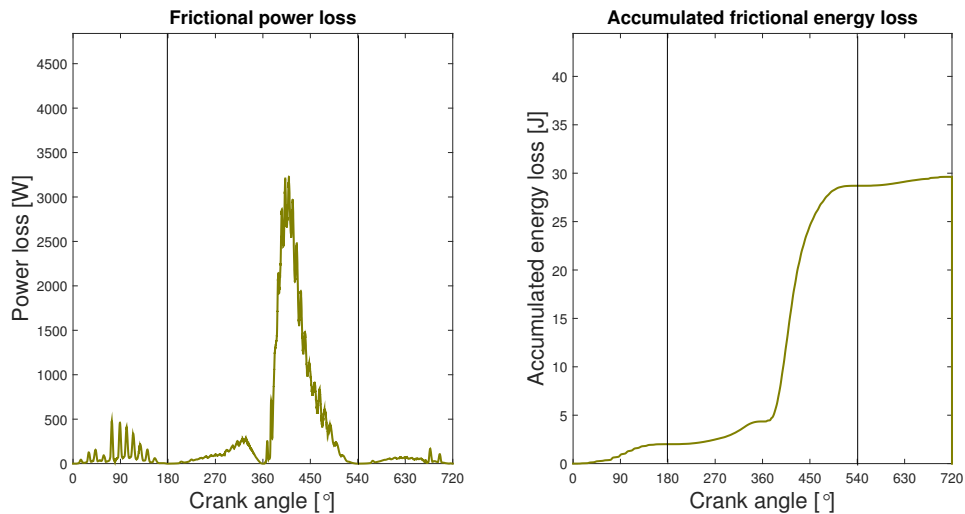


Figure 4.4: Frictional power and energy loss for the piston A during the second combustion cycle.

Where the frictional power loss and energy loss appears during the combustion cycle can be seen in the graphs located in Figure 4.4. Comparing the frictional power loss graph to the graph for the lateral motion in Figure 4.3 a clear correlation can be seen; where the lateral displacement is large frictional power loss occurs. Looking at the graph for the accumulated frictional energy loss it is clear that the largest energy loss occurs during the combustion phase. This is due to the piston skirt dragging against the thrust side of the cylinder liner with a high side force as the piston moves downwards during the combustion phase, and this downstroke is responsible for the vast majority of the energy loss during the combustion cycle.

Observing the graphs in Figure 4.5 it is apparent why the large gradients in the graphs for frictional power loss and accumulated energy loss appear where they do. The graph showing the friction force shows that the vast majority of the friction force occurs on the thrust side when the piston is moving downwards during the combustion phase. Something in common for all the graphs is that they experience the most activity on the thrust side when the combustion pressure is acting on the piston. For the graphs showing the hydrodynamic force and total normal force peaks can also be seen on the anti-thrust side, just before the piston arrives at TDC. These peaks correlate with the lateral movement of the piston towards the anti-thrust side clearly seen in Figure 4.3.

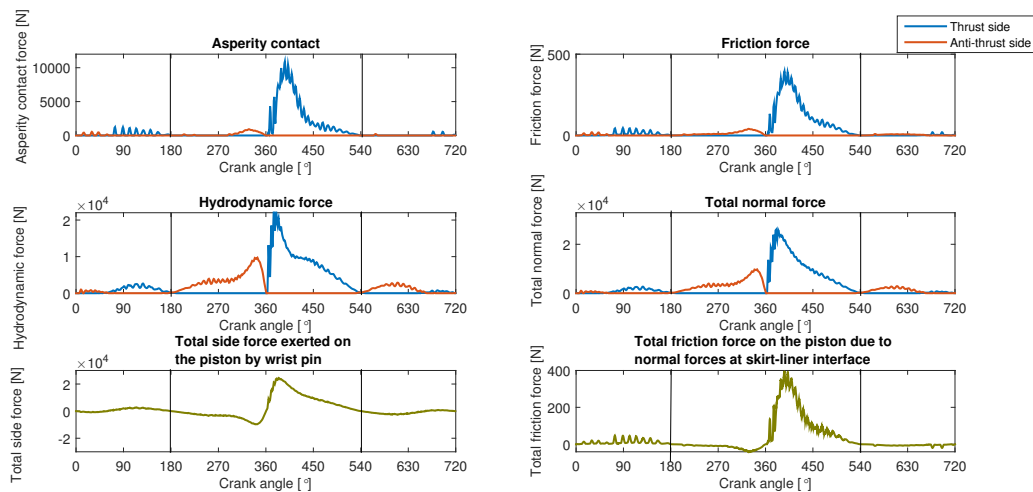


Figure 4.5: Six figures showing asperity contact, hydrodynamic force and frictional force for the piston A for the second combustion cycle. For the graph showing the total side force exerted on the piston by the wrist-pin a negative value corresponds to the side force acting on the anti-thrust side.

4.2.2 Lubrication oil distribution

In this section the oil distribution between the piston skirt and the cylinder liner for Piston A was studied, which can be seen in Figure 4.6 and 4.7.

4. Results

CA: 0 degrees (start of combustion cycle, piston at TDC, about to move downwards) At the start of the combustion cycle it can be seen that the anti-thrust side of the cylinder liner carries a larger quantity of lubrication oil compared to the thrust side, which is also true for the piston skirt and chamfer. The largest quantity of lubrication oil can be found at the bottom of the cylinder liner, but at around a third up on the cylinder liner on the thrust side a pooling of lubrication oil can be seen. At this point the piston is centered in its lateral position, and as a result of that the side force is low.

CA: 60 degrees At 60 degrees the oil amount between piston skirts and cylinder liner is starting to increase, especially on the anti-thrust side where the oil film is thickest at the outer edges of the skirt, whereas on the thrust side the most lubrication oil is found towards the bottom of the piston skirt. The oil quantity in the chamfer has stayed the same and the side force is still relatively low. It can also be seen that as the piston moves downwards, no oil is assumed to be left above. This is the influence of the piston rings which keeps the lubrication oil separated from the combustion chamber.

CA: 120 degrees As the piston continues downwards the lubrication oil amount between piston skirt and cylinder liner is becoming thick over the entire area on the anti-thrust side. On the thrust side the largest quantity between piston skirt and cylinder liner is found on the edges of the piston skirt. Between degrees 60 and 120 the oil level in the chamfer has increased on both sides, and the wrist-pin is now pressing with a force of 2000 N towards the thrust side.

CA: 180 degrees When the piston arrives at BDC the oil levels in the chamfer has increased further on both sides. On the anti-thrust side the amount of oil between piston skirt and cylinder liner is large over the entire piston skirt area, and on the thrust side the majority of the oil between piston skirt and cylinder liner is located towards the edges of the skirt. The side force at this point is virtually non-existent.

CA: 240 degrees As the piston starts to move upwards again it presses against the anti-thrust side of the cylinder liner. The effect of this behavior on the oil distribution is clear to see as the lubrication oil on the anti-thrust side is pressed towards the edges of piston skirt. On the thrust side a pooling of lubrication oil towards the outer edges of the piston skirt has appeared on the cylinder liner, coming from the chamfer as the piston moves upwards. The reduction of lubrication oil in the chamfer can also be seen on the anti-thrust side, but to a slightly smaller extent. As the piston moves upwards the side force is now directed towards the anti-thrust side.

CA: 300 degrees With the piston moving upwards the oil levels in the chamfers on each side keep being reduced to supply the piston skirts with lubrication oil. At this point the oil between the piston skirt and cylinder liner is located almost exclusively towards the edges of the skirt. Compared to the earlier step the side force has increased slightly, and now has a magnitude of roughly 3700 N.

CA: 370 degrees At 370 degrees the piston has arrived at TDC and has started to move downwards. As seen in the middle figure the influence of the combustion pressure can be seen as the piston is heavily deflected towards the thrust side and the side force is increased to 15 kN. At the bottom of the piston skirt on the anti-thrust side the influence of the oil splash can be seen; as the piston arrives at TDC the oil splash is added, which is taken into consideration as the piston moves downwards again.

CA: 420 degrees As the piston keeps moving downwards it keeps on pressing against the thrust side, which prevents the oil film between piston skirt and cylinder liner from becoming thick. However, on the anti-thrust side the influence of the oil splash can clearly be seen as the oil film has become relatively thick. Compared to the oil levels at TDC, the amount of oil in the chamfer has increased slightly. The influence of the combustion pressure on the side force can still be seen clearly as it is still around 14 kN.

CA: 480 degrees When the piston has reached 480 degrees the lubrication oil in the chamfer has kept on being filled, with especially the anti-thrust side chamfer experiencing a large increase in lubrication oil. The effect of the combustion pressure is still seen, with the side force towards the thrust side being roughly 6.5 kN. Due to the piston skirt pressing towards the cylinder liner the oil film on the thrust side between the skirt and the cylinder liner has still not been able to grow, whereas on the anti-thrust side the oil film has grown extremely thick.

CA: 540 degrees As the piston arrives at BDC for the second time during the combustion cycle the chamfer contains a large amount of lubrication oil. Due to the piston moving from thrust side towards anti-thrust side a void in the lubrication oil has been created on the anti-thrust side that will be closed as the piston will keep moving towards the anti-thrust side. On the anti-thrust side the oil film has continued to grow and is now at its thickest during the combustion cycle, whereas the oil film thickness on the thrust side is still comparatively thin. As the piston moves from the thrust side to the anti-thrust side the side force at this point is low once again.

CA: 600 degrees When the piston skirt moves towards the anti-thrust side the lubrication oil is once again pressed towards the piston skirt's edges. The oil level in the chamfer is starting to decrease as it supplies the piston skirt with lubrication oil, and some of this oil is left on the cylinder liner's thrust side as the piston moves towards the anti-thrust side. As the connecting rod is directed towards the anti-thrust side a side force of 2.5 kN is acting towards the anti-thrust side.

CA: 660 degrees At 660 degrees the oil level in the chamfer has decreased even more, and on the anti-thrust side the influence of the barrel shape of the piston skirt can be seen, where the amount of oil between piston skirt and cylinder liner is thickest towards the edges of the piston skirt. The side force has decreased compared to the previous figure, and is approaching zero.

4. Results

CA: 720 degrees As the piston arrives at TDC for the second time to complete the combustion cycle the oil level in the chamfer has decreased even more. The side force is almost non-existent, and the amount of oil between piston skirt and cylinder liner is large on the anti-thrust side, while it is significantly lower on the thrust side. On the anti-thrust side the largest amount of oil between the skirt and cylinder liner can be found at the top part of the skirt. Regarding the oil distribution in the power cylinder unit at the end of the combustion cycle it can be seen that the entire anti-thrust side generally carries more lubrication oil than the thrust side, with the thickest oil film being located at the bottom of the cylinder liner, and the outer edges having more oil than the middle of the anti-thrust side. On the thrust side there is an area about a third of the way up of the piston skirt's movement where the oil film is especially thick. This area of additional lubrication oil comes from the chamfer as it supplied the piston skirt and cylinder liner with oil after the piston was at BDC, and since the piston moves to the anti-thrust side during the upstroke a pooling of lubrication oil is left on the cylinder liner. Comparing 0 degrees and the 720 degrees shows that the two oil distributions differ from each other. This indicates that two combustion cycles are not enough in order for the simulation to reach convergence, but can be used to study the trend of the oil distribution.

Summary of the combustion cycle For the downstroke during the intake-phase the chamfer gets filled on both thrust- and anti-thrust side, and as the piston moves downwards there is assumed to be no oil left on the walls of the cylinder liner above the piston rings. At BDC the chamfer on the anti-thrust side carries more oil than the thrust side, and the amount of lubrication oil between the piston skirt and the cylinder liner on the anti-thrust side is larger than on the thrust side. As the piston moves upwards again it moves slightly to the anti-thrust side, leaving an area of thicker lubrication oil on the thrust side, while the oil level in the chamfers simultaneously decreases. Due to the limited amount of lubrication oil in the chamfer on the thrust side the amount of oil left on the cylinder liner above 240 mm becomes very low, while the cylinder liner on the anti-thrust side maintains a healthy amount of lubrication oil.

As the piston arrives at TDC the combustion pressure will start acting on the piston, and this is shown in a heavy lateral deflection of the piston towards the thrust side, which will be present during almost the entire downstroke. As usual, the chamfers fill up as the piston moves downwards, and at BDC the anti-thrust side has more lubrication oil than the thrust side. When the piston moves upwards the lateral movement towards the anti-thrust side is once again present, which leaves an area with increased lubrication oil in the same place as the previous upwards stroke. Also, as for the previous upwards stroke, the oil levels in the chamfers go down and leaves the cylinder liner on the thrust side with little oil as it once again reaches TDC.

4.2.3 Deformation and pressure distribution

In Figure 4.8 and Figure 4.9 the most interesting part of the combustion cycle with regard to asperity pressure, deformation, and hydrodynamic pressure on the

thrust side is shown, namely the combustion phase. It can be seen that at 360 degrees rotation of the crank shaft the combustion pressure has not yet been able to affect the thrust side of the piston notably, as no asperity pressure, deformation, or hydrodynamic pressure is visible. When the combustion pressure has started acting on the piston it is clear that the largest deformations occur in the middle of the skirt. These deformations are not surprising considering the slight ovality of the piston, and as a result of the ovality the middle of the piston skirt should come in contact first. The deformations become quite large as soon as the combustion pressure builds up, and the largest deformations are seen at crank angle 450.

The hydrodynamic pressure can be seen to be largest at the start of the combustion phase, with a magnitude exceeding 200 bar. During the entire combustion phase the highest hydrodynamic pressures are generally located towards the edges of the skirt. The pattern of the hydrodynamic pressure is likely a result of the deformation area of the piston skirt when it presses against the cylinder liner; at crank angle 390 the pattern takes a circular shape, which could correspond to the peak of the barrel shape coming in contact with the cylinder liner. As the piston skirt deforms more lower part of the skirt comes in contact with the cylinder liner, and the hydrodynamic pressure takes on a more triangular pattern, seen in Figure 4.8 at angle 420. With the piston skirt deforming even more the upper part starts deforming as well, and the barrel shape of the piston skirt can be discerned at crank angle 450.

As can be seen in Figure 4.5 the asperity contact is also the largest during this phase, and by looking at the asperity pressure in Figures 4.8 and 4.9 it can be identified where the asperity contact largely occurs. Looking at the entire downstroke the asperity pressure occurs towards the sides of the piston skirt, and its maximum magnitude reaching 202 bar (not captured in figure for the selected crank angles). It is difficult to establish if the location of this asperity pressure, towards the sides of the piston skirt, is reasonable. Intuitively there should be some asperity pressure in the same area as where the deformation of the piston skirt occurs, but that is not something that can be seen in these figures.

4. Results

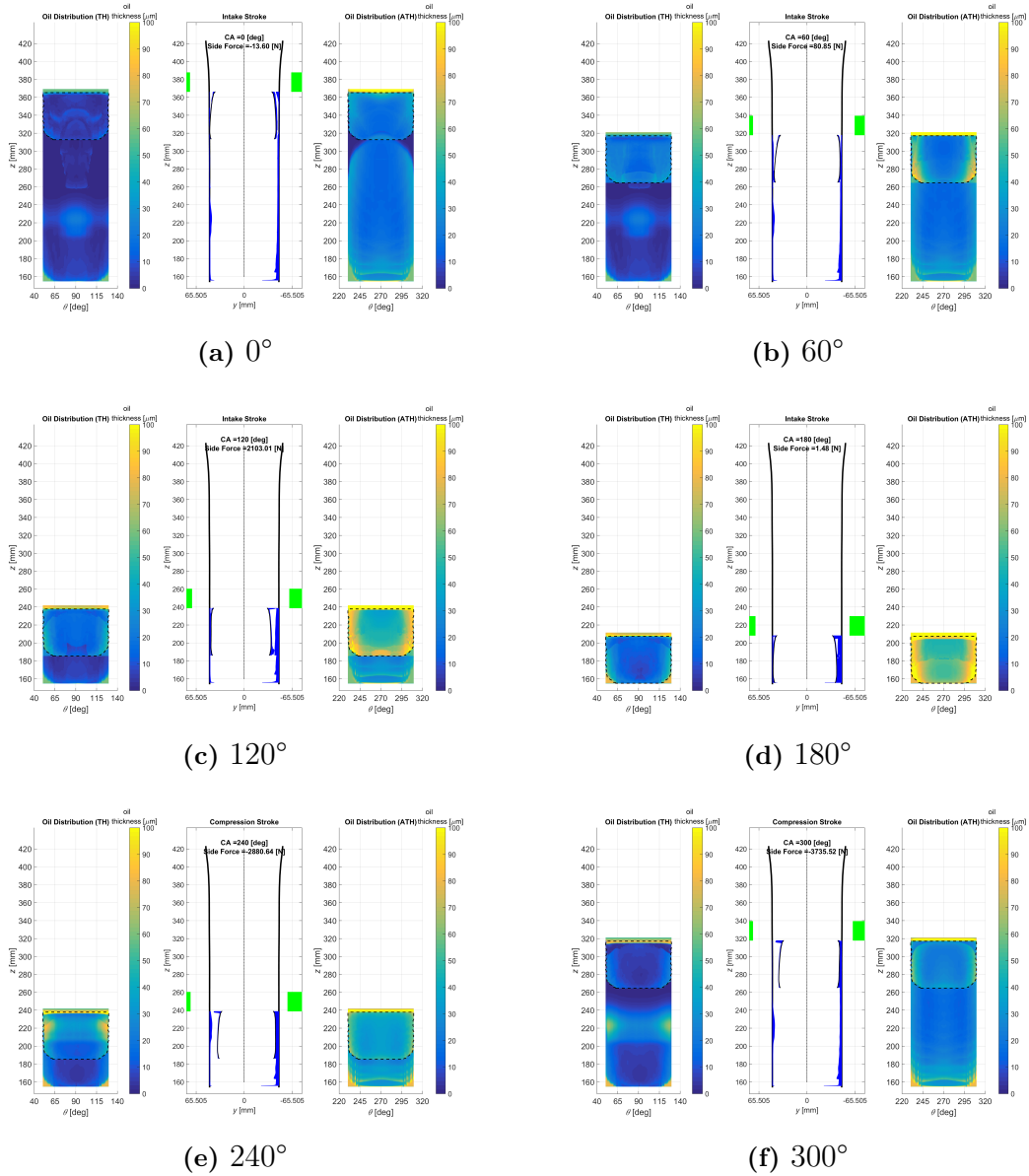


Figure 4.6: Simulation of lubrication oil distribution for the piston A at 1200 rpm at different crank angles in the interval $[0, 300]^\circ$.

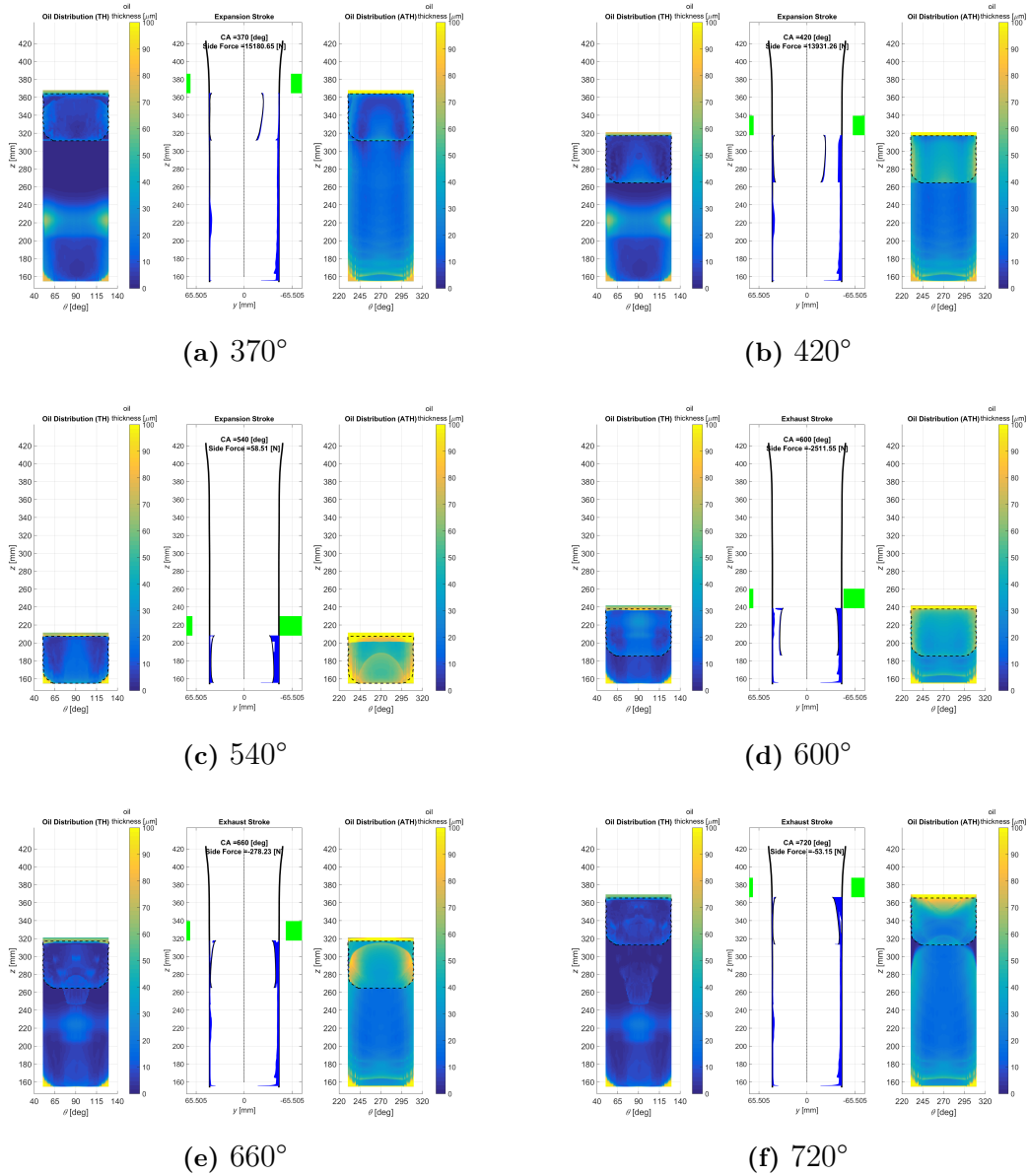


Figure 4.7: Simulation of lubrication oil distribution for the piston A at 1200 rpm at different crank angles in the interval $[370, 720]^\circ$.

4. Results

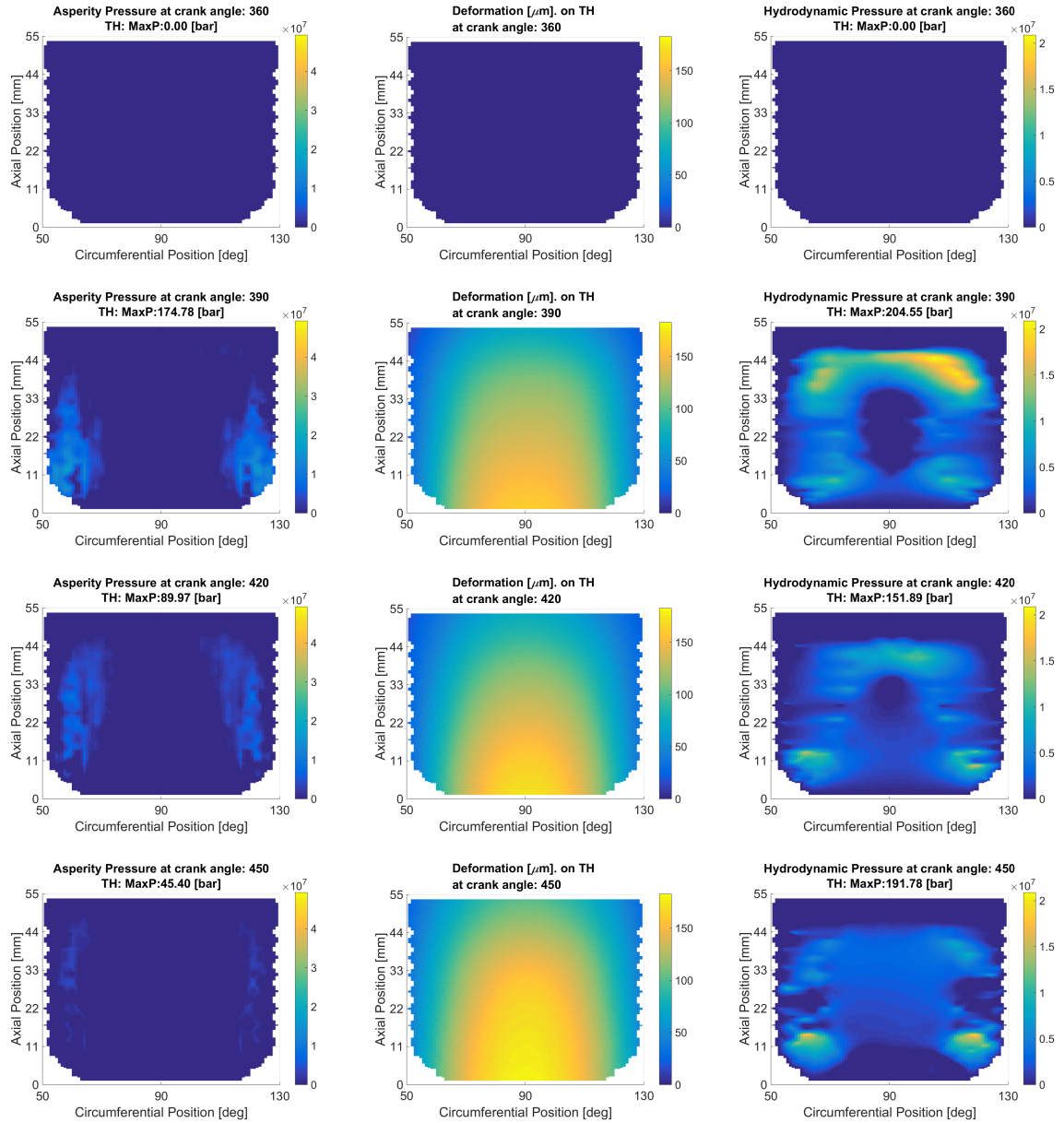


Figure 4.8: Asperity contact pressure (first column), Deformation (second column) and hydrodynamic pressure (third column) on the thrust side on the piston A for the crank angles 360°, 390°, 420° and 450°.

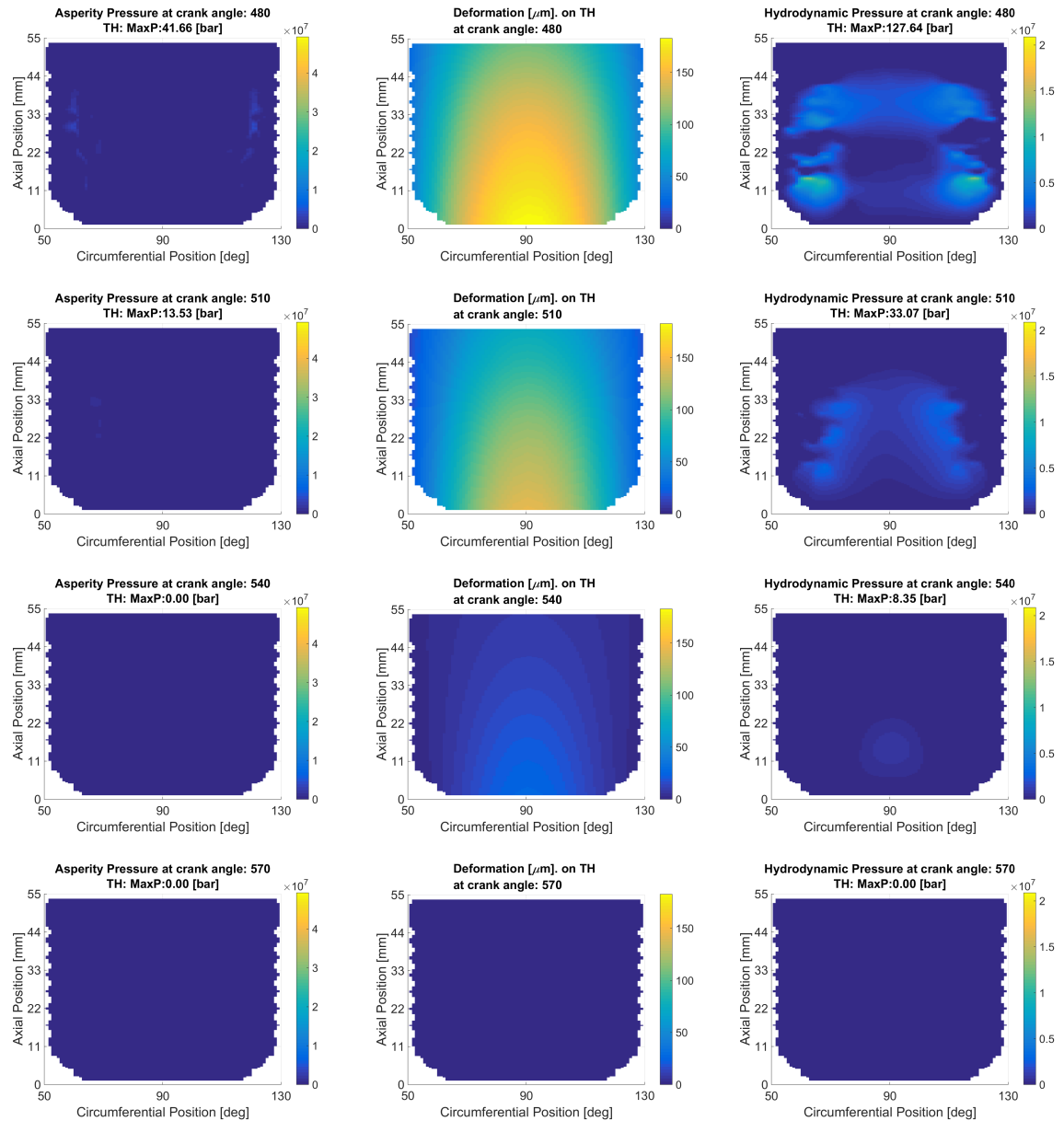


Figure 4.9: Asperity contact pressure (first column), Deformation (second column) and hydrodynamic pressure (third column) on the thrust side on the piston A for the crank angles 480°, 510°, 540° and 570°.

4.3 Piston B

The simulation for the piston B was carried out for an rpm value of 900, which in turn meant that the combustion pressure was lowered compared to the combustion pressure for the piston A, which can be seen in Figure 3.6.

4.3.1 Piston secondary motion and general forces

Regarding the lateral motion of the piston B seen in Figure 4.10 the first thing to be noted is that it is very similar to that of the piston A; the peaks and valleys are located at the same crank angles and the magnitude of the motion is very similar. For the tilting motion, also seen in Figure 4.10, the behavior is also similar to the piston A. The biggest difference is that many of the high-frequency fluctuations seen in the graph for the piston A's tilting motion are reduced or non-existent in the case for the piston B. However, since the piston A and B haven't been simulated for exactly the same input parameters, no definitive conclusions can be drawn from this.

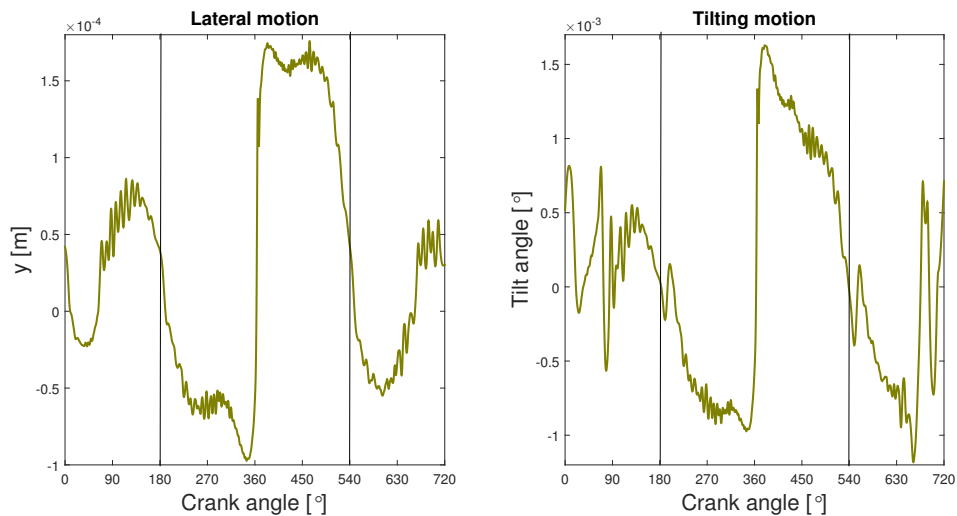


Figure 4.10: Lateral and tilting motion of the piston B during the second combustion cycle.

Looking at the frictional losses in the system for the piston B simulation it can be noted that they are roughly one third of the losses from the simulation of piston A. This is most likely due to the difference in combustion pressure between the two simulations, but also the rpm contributes to the difference. But as mentioned earlier, no definitive conclusions can be drawn.

For the piston B the same characteristics of the force plots can be seen that were present for the piston A simulation. The peaks and valleys arise at the same crank angles and the same behavior between thrust- and anti-thrust side can be seen. Worth noting is that the plots for the asperity contact, friction force, and total friction force on the piston due to normal forces at skirt-liner interface follow the

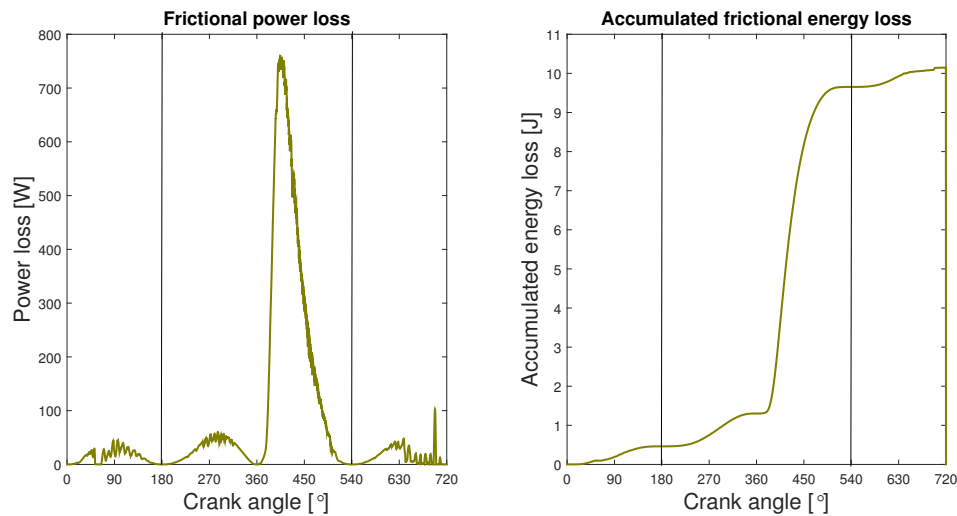


Figure 4.11: Frictional power and energy loss for the piston B during the second combustion cycle.

same relation as the frictional losses, namely that they are roughly one third of their counterparts for the piston A simulation, while the graphs for the hydrodynamic force, total normal force, and total side force exerted on the piston by the wrist-pin are roughly 70% of that of the piston A simulation.

4.3.2 Lubrication oil distribution

For the lubrication oil distribution for the Piston B simulation it can be summarized as being very similar to the lubrication oil distribution for the Piston A simulation. As the piston moves downwards the chamfer fills up with oil on both sides, and as the piston moves upwards it presses against the anti-thrust side.

When the combustion pressure starts to act the piston is pressed against the thrust side with a large side force, and after arriving at BDC again the piston once again presses against the anti-thrust side, leaving an area of increased oil film thickness on the thrust side.

4.3.3 Deformation and pressure distribution

Also in the Figure 4.15 for the asperity pressure, skirt deformation, and hydrodynamic pressure are similar for the piston A simulation. As previously, the figures showing these quantities are of the thrust side of the piston, between crank angles 360 to 570.

It can be seen that once again the asperity pressure is mainly located towards the sides of the skirt when the piston is moving downwards during the combustion phase. The deformation of the piston skirt is largest during the same interval, and the middle part of the skirt deforms the most. For the hydrodynamic pressure it can once again be seen that the most activity is present slightly outside the center of the thrust side piston skirt.

4. Results

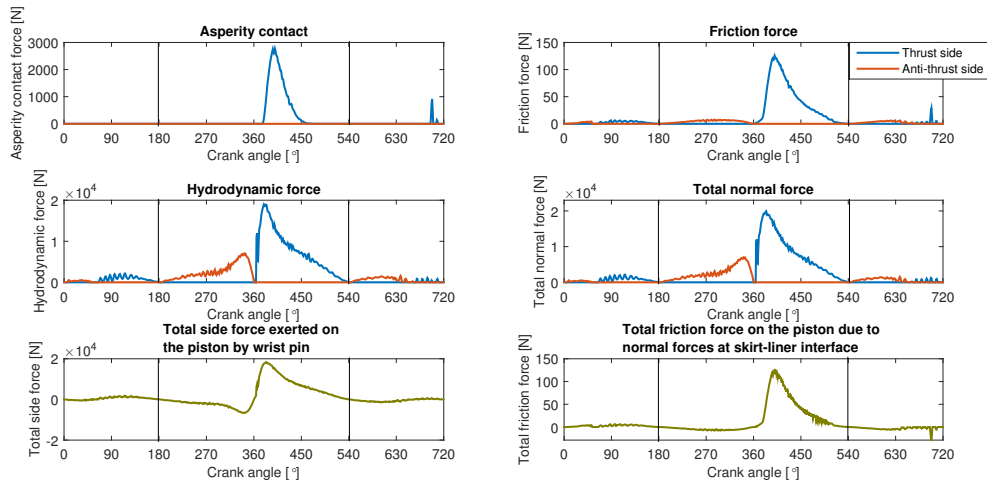


Figure 4.12: Six figures showing asperity contact, hydrodynamic force and frictional force for the piston B for the second combustion cycle. For the graph showing the total side force exerted on the piston by the wrist-pin a negative value corresponds to the side force acting on the anti-thrust side.

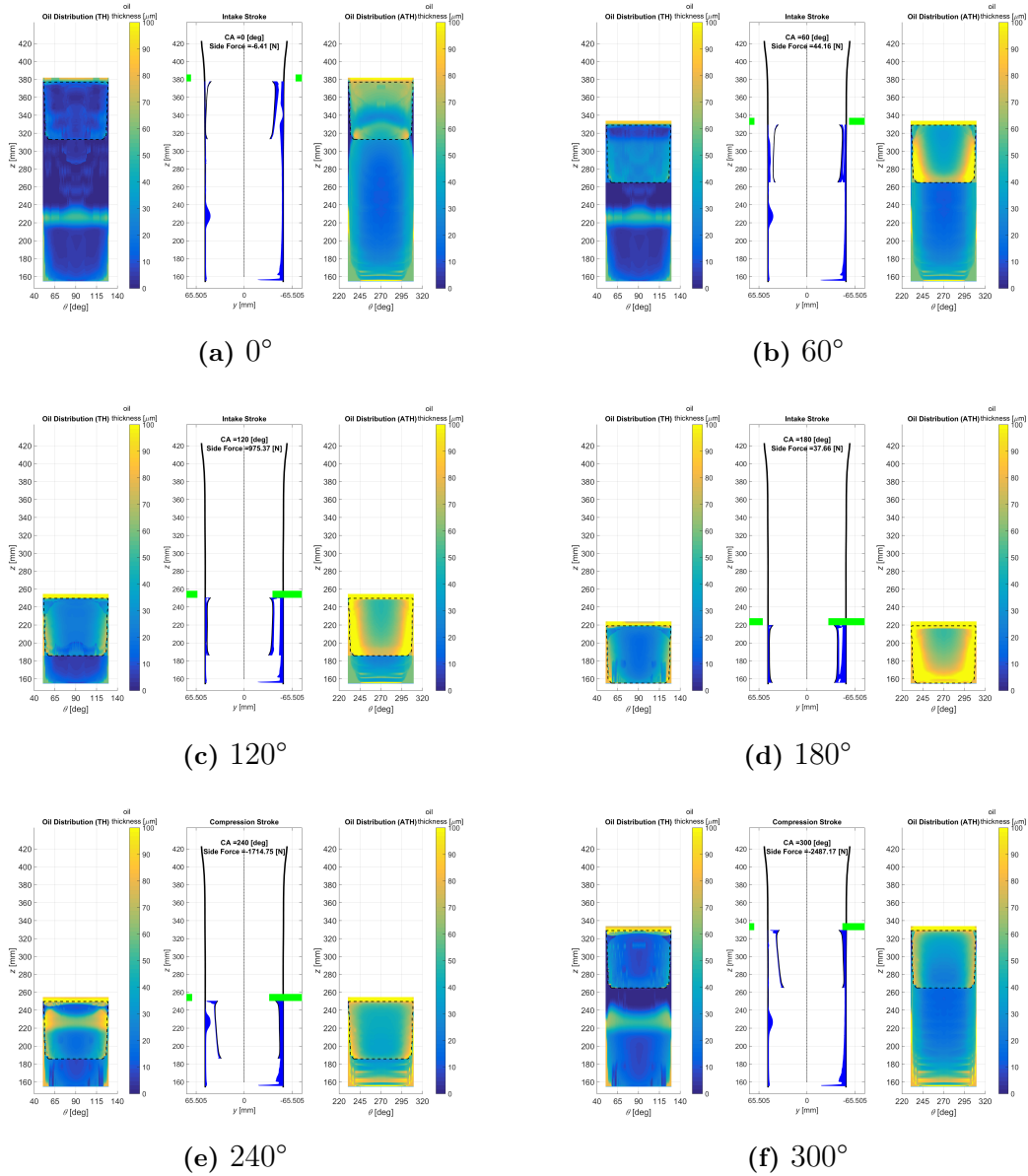


Figure 4.13: Simulation of lubrication oil distribution for the piston B at 900 rpm at different crank angles in the interval $[0, 300]^\circ$.

4. Results

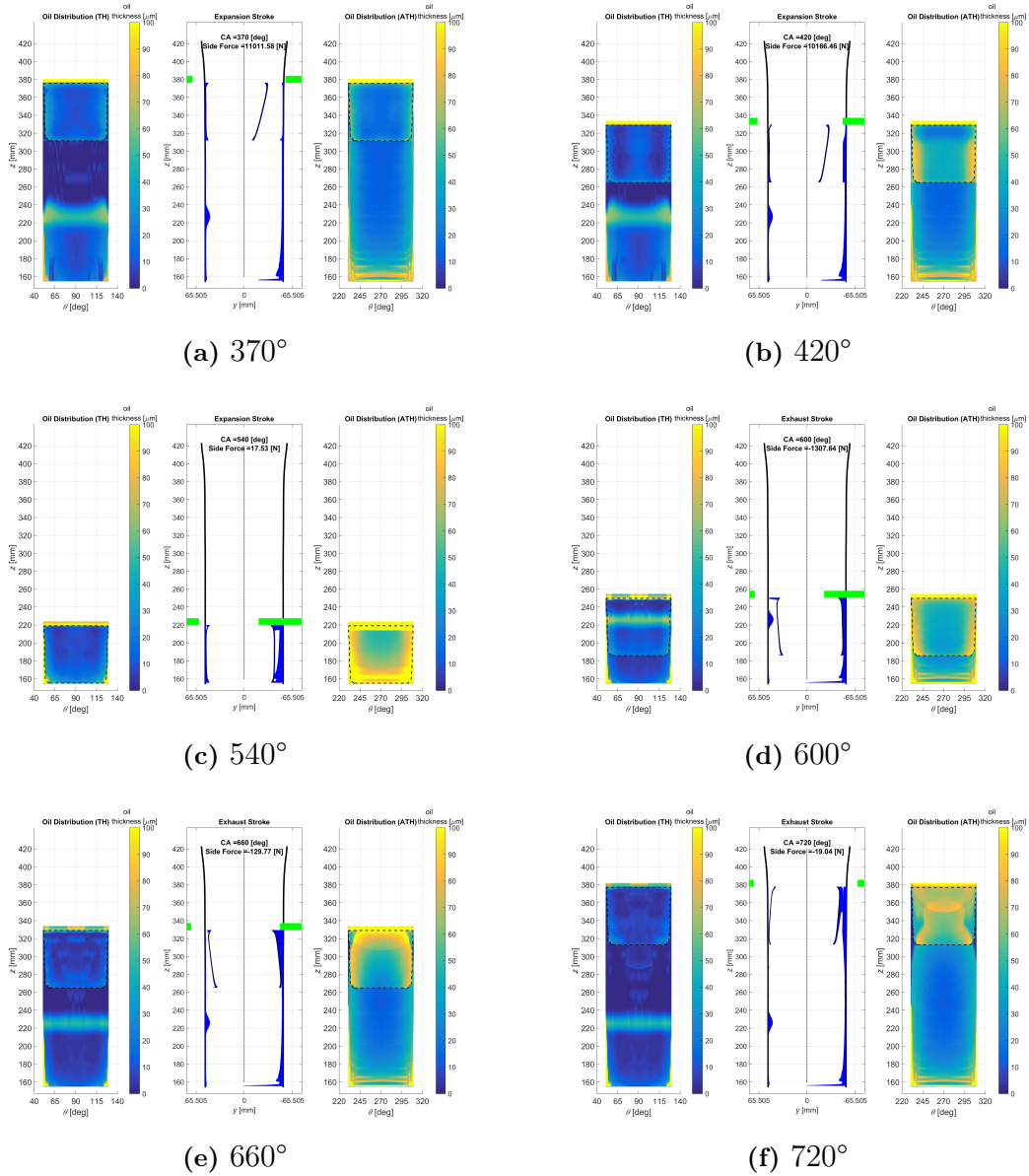


Figure 4.14: Simulation of lubrication oil distribution for the piston B at 900 rpm at different crank angles in the interval $[370, 720]^\circ$.

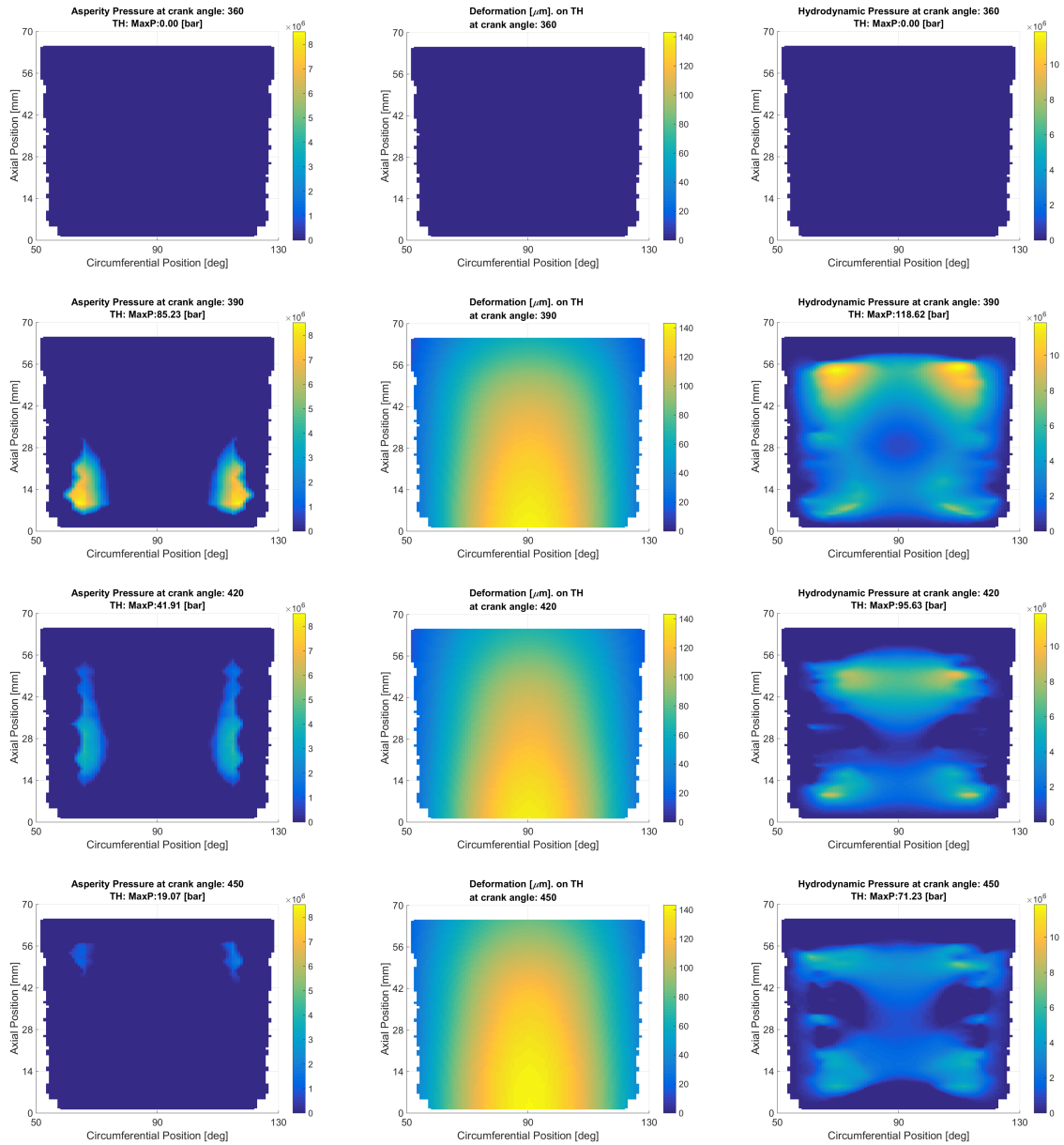


Figure 4.15: Asperity contact pressure (first column), Deformation (second column) and hydrodynamic pressure (third column) on the thrust side on the piston B for the crank angles 360°, 390°, 420° and 450°.

4. Results

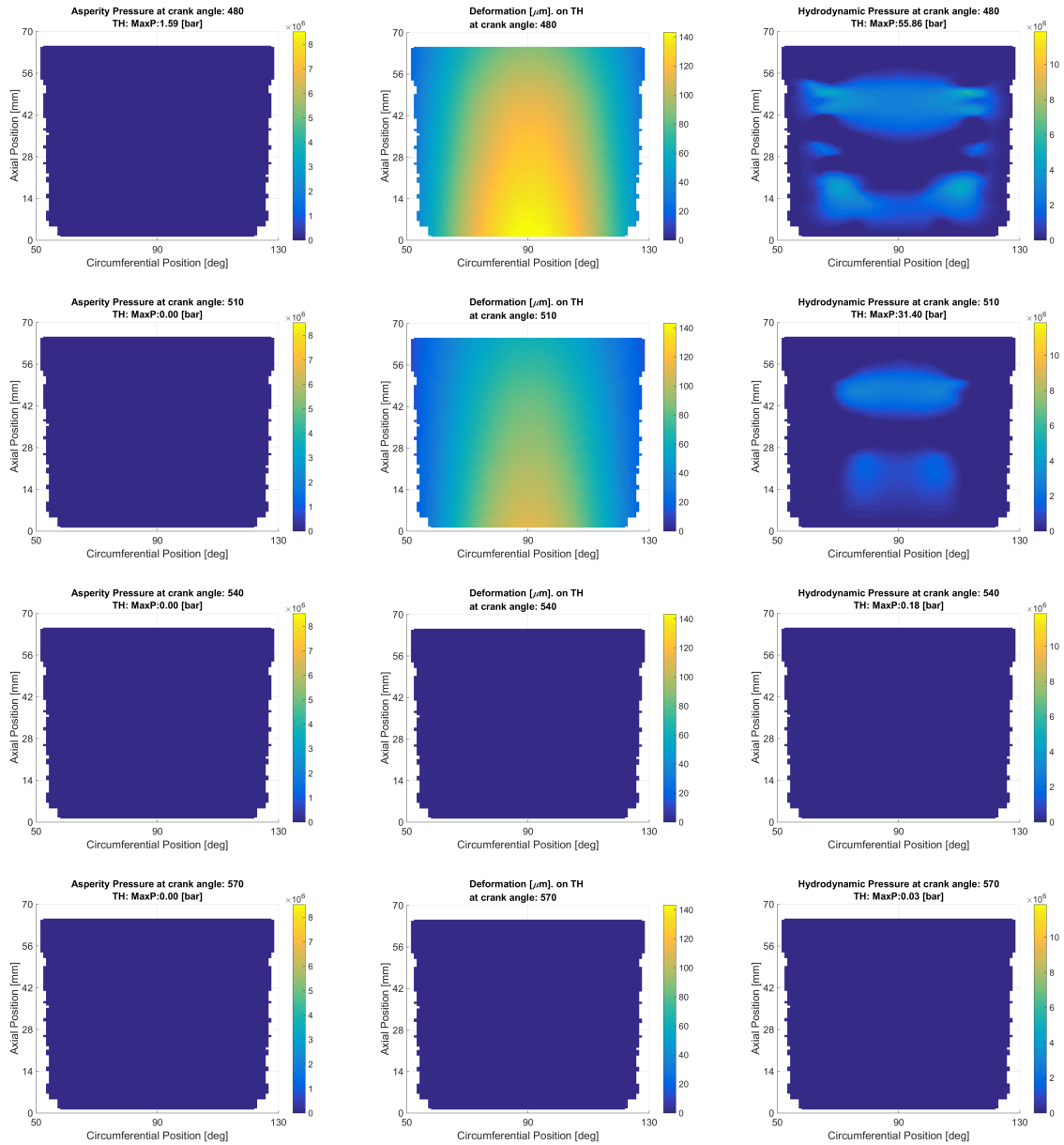


Figure 4.16: Asperity contact pressure (first column), Deformation (second column) and hydrodynamic pressure (third column) on the thrust side on the piston B for the crank angles 480°, 510°, 540° and 570°.

4.4 Influence of combustion pressure, engine speed, oil splash, and tooling marks

In this section the results of the influence of combustion pressure, engine speed, oil splash, and wave height will be presented. The shape of the piston skirt that these results correspond to differs slightly to the shape on the piston in reality, in that it has a vertical notch in the center of the piston skirt. This difference in piston skirt geometry changes the lubrication oil distribution, which of course will influence other outputs, but the simulations are still considered to be of interest when looking at the different parameters' effect on piston secondary motion, frictional losses, and forces in the mechanical system. The results presented are taken from the second combustion cycle of the simulations.

4.4.1 Combustion pressure and engine speed parameterization

For the engine speed parameterization three different values were chosen: 900, 1200, and 1800 rpm. The difference in rpm not only changes the speed at which the piston moves up and down in the cylinder, but also correspond to different combustion pressures, see Figure 3.6. In this figure it can be seen that 1200 rpm corresponds to the highest combustion pressure, and that the combustion pressure for 1800 rpm is higher than the combustion pressure for 900 rpm.

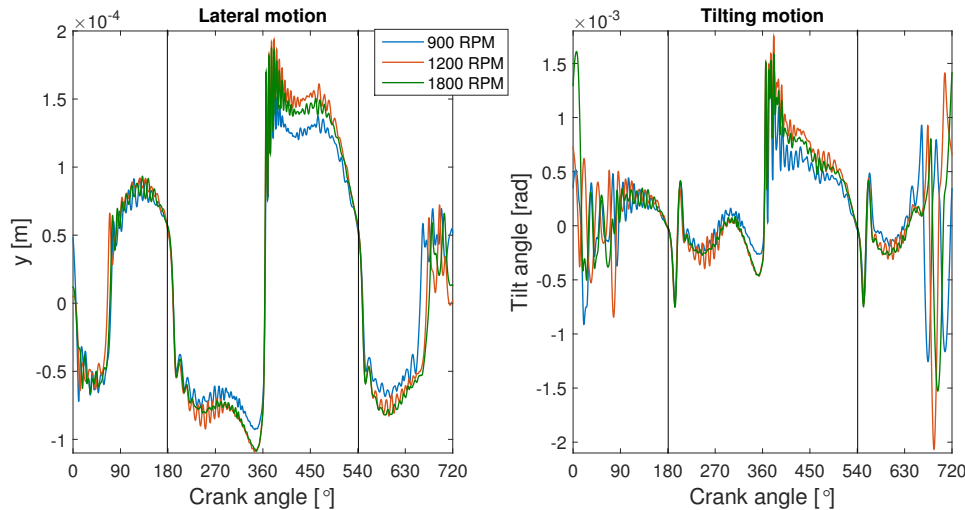


Figure 4.17: Lateral and tilting motion for the piston B for 900, 1200, and 1800 rpm.

Looking at the lateral motion of the piston for the rpm-parameterization in Figure 4.17 it can be noted that peaks and valleys are located at the same crank angles for all three simulations, from which it can be concluded that no significant phase shift is induced when changing the revolution speed and combustion pressure. However, the magnitude of lateral movement seems to be the largest for the 1200

4. Results

rpm-simulation, second highest for the 1800 rpm-simulation and lowest for the 900 rpm-simulation, which is particularly prominent when the combustion pressure acts on the piston around crank angle 360. The order of these correlate with the peak combustion pressure where the combustion pressure for 1200 rpm was the highest, and the combustion pressure for 900 rpm the lowest.

Overall, the differences between rpm simulations are more clearly seen in the graph for the lateral motion in Figure 4.17 compared to the tilting motion, but the general behavior is roughly the same for all three simulations in both graphs. The most prominent differences are once again seen when the combustion pressure is applied to the piston. The magnitudes of the tilting angle for the different simulations are in the same order as for the lateral motion, and thus also correlate with the magnitude of the combustion pressure, where the largest combustion pressure peak gives the largest piston secondary motion, both with regard to lateral motion and tilting angle.

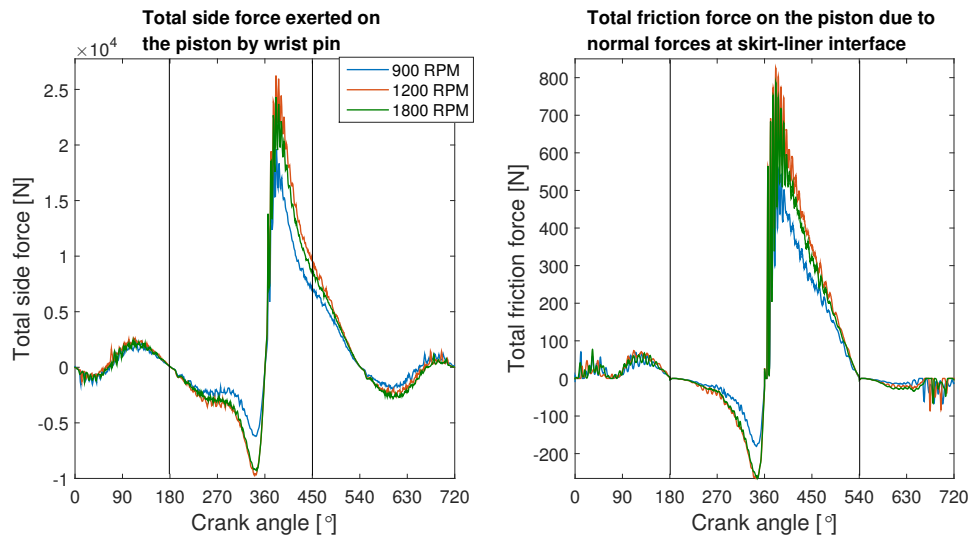


Figure 4.18: Total side and friction forces for the piston B for 900, 1200, and 1800 rpm.

The graphs for the total side force exerted on the piston by the wrist pin and the total friction force on the piston due to normal forces at skirt-liner interface seen in Figure 4.18 follow the same behavior as the piston secondary motion, namely that the higher the combustion pressure, the higher these magnitudes become. This seems reasonable since a higher pressure will lead to larger lateral forces, and thus the side force exerted on the piston by the wrist pin and the friction force should increase. An interesting phenomenon for these graphs is that a difference in magnitudes can be seen before the combustion pressure acts on the piston, around 240-360 degrees on the crank angle. The reason for this difference is unclear, but could be due to the difference in vertical velocity for the different engine speed values, and the subsequent difference in acceleration. It could also be due to the pressures in the PCU being slightly different for different rpm values outside of the combustion phase (see Figure 3.6).

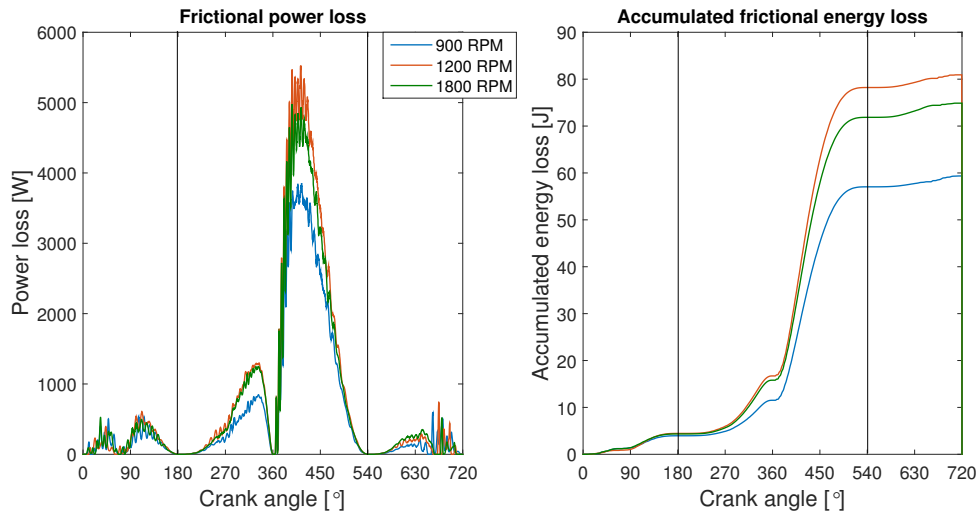


Figure 4.19: Frictional power and accumulated frictional energy loss for the piston B for 900, 1200, and 1800 rpm.

Lastly, the influence of the combustion pressure and rpm can be seen in Figure 4.19 where a clear correlation can be seen between increased combustion pressure and accumulated frictional loss. Before the combustion phase the accumulated frictional energy loss is at around 15 J for all three simulations, but range between 80 J and 60 J after the combustion phase. It can therefore be concluded that the difference in combustion pressure and rpm has the largest influence during the crank angle degrees 360 to 540.

4.4.2 Oil supply parameterization

For the oil supply parameterization three different oil splash values were simulated at 1200 rpm: 20, 30, and 40 μm . The oil splash is added uniformly to the cylinder liner surface that is located below the piston skirt when the piston is at TDC.

Looking at the piston secondary motion for the oil splash parameterization in Figure 4.20 it can be seen that the oil splash has a minimal effect on the lateral movement of the piston. The graphs are largely positioned on top of each other, except for when the piston moves heavily to the anti-thrust side, around crank angles 230 and 590. For the tilting motion there seems to be a correlation between the oil splash and the magnitude of the tilting motion fluctuations. For the highest oil splash the fluctuations seem to be lower, while for the lowest oil splash the fluctuations seem to be the largest, which indicates that the added lubrication oil might have a damping effect on the tilting movement of the piston.

The effect the oil splash has on the total side force exerted on the piston by the wrist pin, seen in Figure 4.21, looks to be close to non-existent as no major differences between the simulations can be seen. At the larger peak in the graph depicting the total friction force a small difference between the simulations might be distinguished where the simulation with the lowest oil splash has a slightly higher total friction force, and the largest oil splash has a slightly lower total friction force.

4. Results

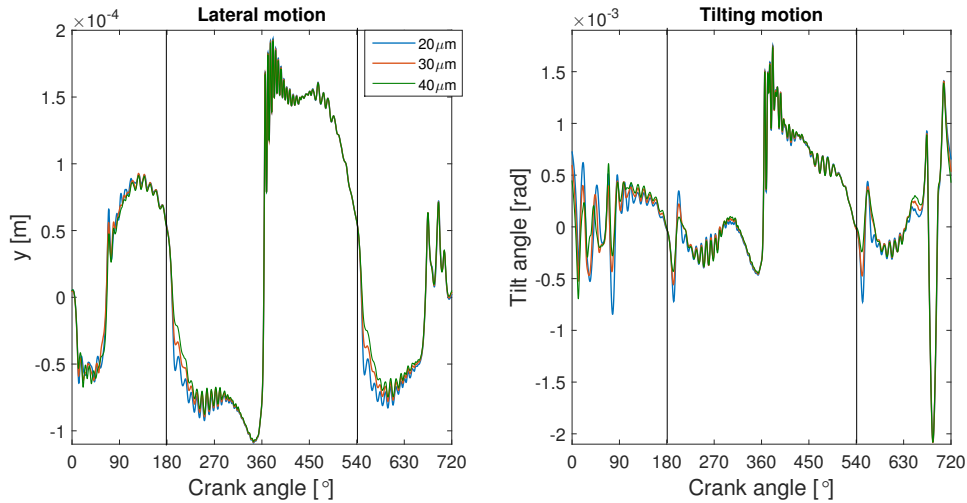


Figure 4.20: Piston secondary motion for oil splash values of 20, 30, and 40 μm .

The graphs in Figure 4.22 showing the frictional losses further reinforces the behavior that could be distinguished in the graphs for the total friction force; namely that the frictional loss is higher for a lower oil splash. This is most clearly seen in the graph for the accumulated frictional energy loss where a clear correlation between oil splash and energy loss can be identified.

Summarized, a thicker oil film on the cylinder liner seems to dampen some of the fluctuations present in the tilting motion. It also reduces the friction during operation which manifests itself in a lower frictional energy loss. The reason for this is likely to be that when the piston moves in its secondary directions, it has a harder time penetrating the oil film, and as a result the amount of asperity contact is reduced.

4.4.3 Tooling marks parameterization

Lastly, for the tooling marks parameterization, three wave heights were investigated: 6, 11, and 16 μm .

By looking at the graphs in Figure 4.23, showing the piston secondary motion, the wave height parameter does not seem to influence the motions to any large extent. The largest difference can be seen at the start of the combustion cycle in the graph showing the tilting motion, but for the rest of the combustion cycle the differences are minimal, both for the lateral motion and the tilting motion.

Figure 4.24 showing the total side force exerted on the piston by the wrist pin and the total friction force on the piston due to normal forces at skirt-liner interface shows an interesting phenomenon; the total side force exerted on the piston by the wrist pin is more or less the same for all three simulations, while the total friction force increases with an increased wave height parameter.

In Figure 4.25 the influence of the wave height parameter can be seen even more clearly. In the graph for the frictional power loss the losses are higher for the larger wave height parameters, and the difference in energy loss between the simulations

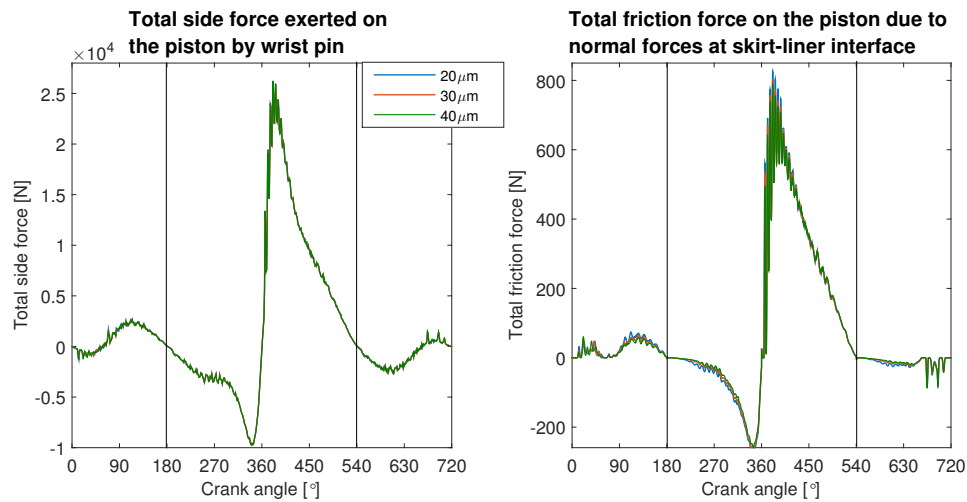


Figure 4.21: Total side force exerted on the piston by the wrist pin and total friction force on the piston due to normal forces at skirt-liner interface for oil splash values of 20, 30, and 40 μm .

is very apparent. As can be seen in the graph for the accumulated frictional energy loss the difference between the simulations increases each time there is a jump in frictional energy loss (around crank angles 120, 260, and 380), meaning that the wave height parameter has an influence during the entire combustion cycle, which is reasonable considering that the piston skirt comes in contact with the cylinder liner several times during the combustion cycle.

4. Results

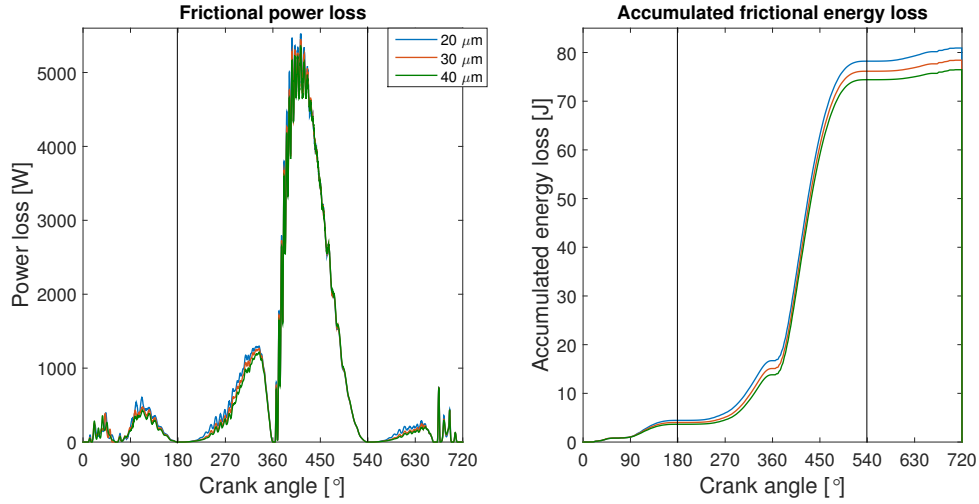


Figure 4.22: Frictional power and accumulated frictional energy loss for the piston B for oil splash values of 20, 30, and 40 μm .

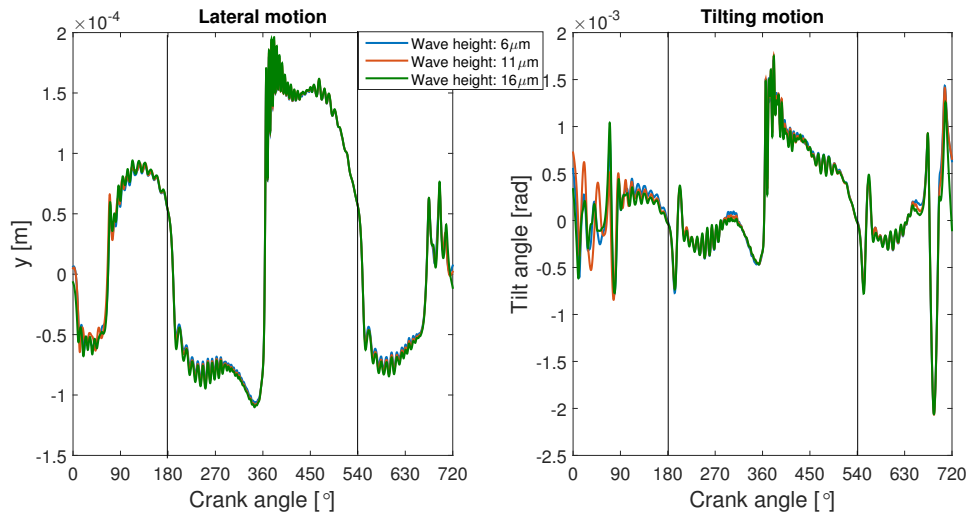


Figure 4.23: Piston secondary motion of the piston B for wave heights of 6, 11, and 16 μm .

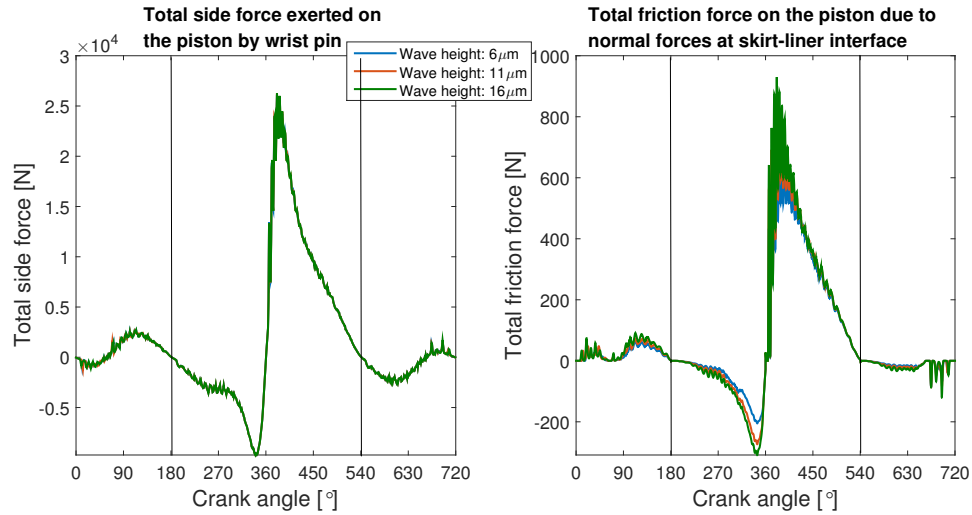


Figure 4.24: Total side force exerted on the piston by the wrist pin and total friction force on the piston due to normal forces at skirt-liner interface for wave heights of 6, 11, and 16 μm .

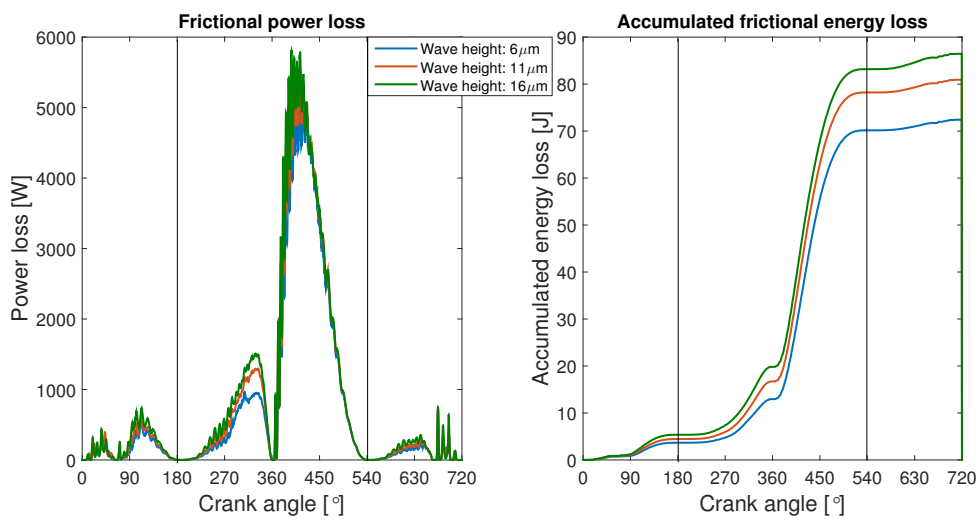


Figure 4.25: Frictional losses for wave heights of 6, 11, and 16 μm .

4.5 Validation of the results

By looking at the side forces $F_{y_{wp2ps}}$ throughout all the results, the highest magnitudes can be seen to be around 17-27kN which is likely due to the relatively high combustion pressure. The highest side forces can thus be seen for the simulations performed with 1200 rpm. The side forces can be compared with the results from another study, *The Effects of Piston Skirt Profiles on Secondary Motion and Friction* [2], where the study is performed for 1680 rpm with a combustion pressure magnitude of approximately 180 bar, which is in between the lowest and highest maximum combustion pressure which this master's thesis uses. The side forces in *The Effects of Piston Skirt Profiles on Secondary Motion and Friction* reach a maximum value of almost 20kN (Figure 4.26) which indicates that the obtained side forces with magnitudes of 17-27kN in this master's thesis are reasonable. In addition to the similarity between the magnitudes, the similarity of the general trends look very promising, which can be seen when comparing Figure 4.26 to e.g. one of the figures 4.18, 4.21, or 4.24.

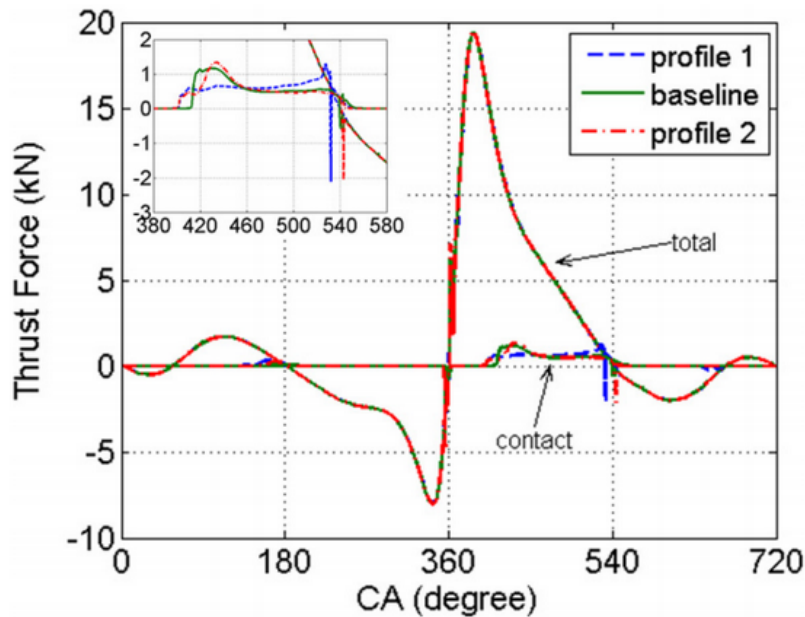


Figure 4.26: The side forces from the study *The Effects of Piston Skirt Profiles on Secondary Motion and Friction* [2]. Note: Commonly one refers to the side forces when the forces are allowed to be negative and positive which means that they are directed in the opposite direction relative to the defined coordinate system. With that said, this figure basically shows the actual normal forces, and thus, they can be compared with the side forces obtained in this master's thesis. E.g. see the figures 4.18, 4.21 and 4.24 for comparison.

The largest magnitudes of the piston secondary motion peaks at approximately 0.16mm and $1.5 \cdot 10^{-3} \text{rad}$ ($\approx 0.086^\circ$) for the lateral and tilting motion, respectively.

How these results stand against real measurements can be compared with *Technique of Measuring Piston Secondary Motion Using Laser Displacement Sensors* [4] where the maximum lateral motion is $\approx 0.4\text{mm}$ and maximum tilting angle is 0.6° for 500rpm. The difference between the simulation results and the results in the study [4], is probably due to the fact that we are comparing two different power cylinder units, which is typically the case when looking for other studies to compare simulation results with. Every study uses their own power cylinder unit which makes it hard to make an exact comparison of the results from this master's thesis with results from other studies.

4. Results

5

Conclusions and future work

The results that were obtained showed great promise. Magnitudes and trends of obtained quantities were reasonable, both compared to similar studies and what was previously known by Volvo GTT Powertrain. A result that might be a bit peculiar is the location of the asperity pressure that is located more towards the sides of the piston skirts instead of in the middle, where they intuitively should be present. Other than that the results were plausible, with larger forces acting on the thrust side than the anti-thrust side, and the relation between them being of reasonable size.

The parameterizations that were carried out also gave satisfactory results, as the parameterizations showed trends that were deemed intuitively sensible, even though they were carried out on piston skirts slightly different from the real pistons.

A way to further validate the results would be of great importance. If experiments regarding the piston secondary motion was carried out, these could be compared to the results from the computational simulations to see if the same trends occur.

The boundary conditions for the cylinder liner FEM simulation also needs to be reviewed. By only clamping the liner at the top it allows for a substantial amount of horizontal movement further down the cylinder liner, which does not appear in the real life system. Restricting the cylinder liner a bit more in the horizontal direction should give more accurate results with respect to piston secondary motion, forces, oil distribution and deformations.

With that said, the software shows great promise regarding its ability to predict the piston secondary motion, friction, and lubrication oil distribution in power cylinder units and, with small tweaks and improvements, has the possibility of becoming a strong and useful tool in analyzing power cylinder units.

5. Conclusions and future work

Bibliography

- [1] F. McClure. *Numerical Modeling of Piston Secondary Motion and Skirt Lubrication in Internal Combustion Engines*. Massachusetts Institute of Technology, September 2007.
- [2] O. Akalin O. Gunelsu. *The Effects of Piston Skirt Profiles on Secondary Motion and Friction*. Mechanical Technical University, Istanbul Technical University, June 2014.
- [3] P. Totaro. *Modeling Piston Secondary Motion and Skirt Lubrication with Applications*. Massachusetts Institute of Technology, June 2014.
- [4] Z.M. Ripin Y-C. Tan. *Technique of Measuring Piston Secondary Motion Using Laser Displacement Sensors*. School of Mechanical Engineering, Universiti Sains Malaysia, February 2012.
- [5] D. Bai. *Modeling Piston Skirt Lubrication in Internal Combustion Engines*. Massachusetts Institute of Technology, June 2012.
- [6] K.L. Johnson. *Contact mechanics*. Cambridge University Press, 1985.
- [7] Y. Wakuri T. Hamatake M. Soejima T. Kitahara. *Piston ring friction in internal combustion engines*. Butterworth-Heinemann Ltd, 1992.

Bibliography

A

Mathematical variables

Table A.1: Summary of the stated mathematical terms in order of apperence in the thesis.

$F_{y_{cb}}$	[N]	The force in the y-direction from the cylinder liner to the piston.
$F_{y_{wp2ps}}, F_{z_{wp2ps}}$	[N]	The forces in the y- and z- direction from the wrist pin to the piston.
F_{y_p}	[N]	The lateral force of the combustion force in the y-direction due to the piston tilting angle ϕ .
L_{CR}	[m]	The length of the connecting rod.
β	[rad]	The connecting rod angle.
$\ddot{\beta}$	[rad·s ⁻²]	The angular acceleration of β .
$Y_{crcg/Q}, Z_{crcg/Q}$	[m]	The location of the center of gravity with respect to a arbitrary point Q (preferable set to the center of the crank pin of the crankshaft) for the connecting rod when β is nonzero.
m_{cr}, m_{wp}, m_{ps}	[kg]	The mass of the connecting rod big-end (bearing), wrist pin and piston, respectively.
a_{crcgy}, a_{crcgz}	[m·s ⁻²]	The acceleration of the connecting rod in the y and z direction respectively, with respect to the center of gravity.
a_{py}	[m·s ⁻²]	The acceleration of the piston in the y-direction.
I_{cr}	[kg·m ²]	The inertia of the connecting rod with respect to its center of gravity.
ϕ	[rad]	The piston tilting angle.
$\dot{\phi}$	[rad·s ⁻¹]	The angular velocity of the piston around it's wrist pin.
$\ddot{\phi}$	[rad·s ⁻²]	The angular acceleration of the piston around it's wrist pin,.
T_{pcom}	[N·m]	The moment acting on the piston relative to the center of gravity from the combustion pressure.
T_{cb}	[N·m]	The moment acting on the piston relative to the center of gravity from the interaction between the cylinder liner and piston.
$Z_{psc/P}, Y_{psc/P}$	[m]	The positions of the piston's center of gravity when $\phi \neq 0$.
ρ	[kg·m ⁻³]	The density of the oil.
u_i, u_j	[m·s ⁻¹]	The velocity of the oil flow stated in tensor form.
$t, \Delta t$	[t]	Time and Time difference.
τ_{ij}	[Pa]	The deviatoric stress tensor.
x_i, x_j	[m]	The directions stated in tensor form. E.q. these can be seen in expression like $\frac{\partial[\text{Arbitrary function}]}{\partial x_i}$ which can be understood as "the partial derivative in the direction of x_i ".

A. Mathematical variables

h	$[\mu\cdot\text{m}]$	The clearance between the cylinder-liner and the piston.
h_{asp}	$[\mu\cdot\text{m}]$	Defined as half of the wave height of the tooling marks.
μ	$[\text{Pa}\cdot\text{s}]$	The dynamic viscosity of the oil.
U	$[\text{m}\cdot\text{s}^{-1}]$	The piston sliding speed $\in [0, 10] \text{ m}\cdot\text{s}^{-1}$
Φ	$[\text{Pa}]$	Representation of pressure.
F'	$[-]$	Indicator variable.
P_{ref}	$[\text{Pa}]$	Reference pressure.
ρ_{ref}	$[\text{kg}\cdot\text{m}^{-3}]$	Reference density of the oil.
$\text{FVEC}(X)$	$[-]$	The function vector consisting of all governing equations that aims to be solved approximately.
J	$[-]$	The Jacobian.
V_{py}^i	$[\text{m}\cdot\text{s}^{-1}]$	The piston sliding speed in the y-direction stated in a discrete form in order to use Newton's method.
x_{py}^i, x_{py}^{i-1}	$[\text{m}]$	The position of the piston in y-direction stated in a discrete form in order to use Newton's method.
ϕ^i, ϕ^{i-1}	$[\text{rad}]$	The piston tilting angle stated in a discrete form in order to use Newton's method.
$\dot{\phi}^i$	$[\text{rad}\cdot\text{s}^{-1}]$	The velocity of the piston tilting angle stated in a discrete form in order to use Newton's method.
C	$[\text{Pa}^{-1}]$	The compliance matrix.
F_0	$[\text{N}]$	The force field.
d_0	$[\mu\cdot\text{m}]$	An initial guessed deformation.
P_{asp}	$[\text{Pa}]$	The pressure when asperity contact is obtained.
A_1, A_2	$[-]$	Constants in the model for the asperity contact.
$\delta = h_{\text{asp}} - h$	$[\mu\cdot\text{m}]$	Difference between the clearance when asperity contact is reached and the clearance.
E_1, E_2	$[\text{Pa}]$	The Young's modulus for two materials which comes into play when asperity contact is reached.
E	$[\text{Pa}]$	The model for the new Young's modulus when asperity contact is reached according to equation (2.12).
ν_1, ν_2	$[-]$	Poisson's ratio for two materials which comes into play when asperity contact is reached.